



Temporal single-cell atlas of non-neuronal retinal cells reveals dynamic, coordinated multicellular responses to central nervous system injury

Received: 14 June 2022

Accepted: 13 January 2023

Published online: 20 February 2023

 Check for updates

Inbal Benhar ^{1,2,11} ✉, Jiarui Ding ^{1,3,11}, Wenjun Yan ⁴, Irene E. Whitney⁴, Anne Jacobi^{4,5,6}, Malika Sud ¹, Grace Burgin¹, Karthik Shekhar^{1,7}, Nicholas M. Tran^{4,8}, Chen Wang^{5,6}, Zhigang He ^{5,6}, Joshua R. Sanes^{4,12} & Aviv Regev ^{1,9,10,12} ✉

Non-neuronal cells are key to the complex cellular interplay that follows central nervous system insult. To understand this interplay, we generated a single-cell atlas of immune, glial and retinal pigment epithelial cells from adult mouse retina before and at multiple time points after axonal transection. We identified rare subsets in naive retina, including interferon (IFN)-response glia and border-associated macrophages, and delineated injury-induced changes in cell composition, expression programs and interactions. Computational analysis charted a three-phase multicellular inflammatory cascade after injury. In the early phase, retinal macroglia and microglia were reactivated, providing chemotactic signals concurrent with infiltration of CCR2⁺ monocytes from the circulation. These cells differentiated into macrophages in the intermediate phase, while an IFN-response program, likely driven by microglia-derived type I IFN, was activated across resident glia. The late phase indicated inflammatory resolution. Our findings provide a framework to decipher cellular circuitry, spatial relationships and molecular interactions following tissue injury.

Tissues vary in their healing and regeneration capacity. Changes in cell states, compositions and interactions affect healing both positively and negatively. In particular, the adult mammalian central nervous system (CNS) extensively remodels after insult yet generally fails to regenerate. Immune cells and glia help orchestrate CNS repair, but their responses to insult are often insufficient and at times counterproductive^{1–3}.

While much has been learned about each cellular component, our understanding of the multicellular networks underlying CNS pathology is more limited^{3–5}.

Optic nerve crush (ONC) injury is a model for studying neuron-intrinsic and neuron-extrinsic processes of CNS degeneration and regeneration⁶. In ONC, the axons of retinal ganglion cells

¹Broad Institute of MIT and Harvard, Cambridge, MA, USA. ²Department of Systems Immunology, Weizmann Institute of Science, Rehovot, Israel.

³Department of Computer Science, University of British Columbia, Vancouver, British Columbia, Canada. ⁴Department of Molecular and Cellular Biology and Center for Brain Science, Harvard University, Cambridge, MA, USA. ⁵F.M. Kirby Neurobiology Center, Boston Children's Hospital, Harvard Medical School, Boston, MA, USA. ⁶Department of Neurology, Harvard Medical School, Boston, MA, USA. ⁷Department of Chemical and Biomolecular Engineering, Helen Wills Neuroscience Institute, University of California, Berkeley, Berkeley, CA, USA. ⁸Department of Molecular and Human Genetics, Baylor College of Medicine, Houston, TX, USA. ⁹Howard Hughes Medical Institute, Department of Biology, Massachusetts Institute of Technology, Cambridge, MA, USA. ¹⁰Present address: Genentech, South San Francisco, CA, USA. ¹¹These authors contributed equally: Inbal Benhar, Jiarui Ding.

¹²These authors jointly supervised this work: Joshua R. Sanes, Aviv Regev. ✉e-mail: inbal.benhar@gmail.com; aviv.regev.sc@gmail.com

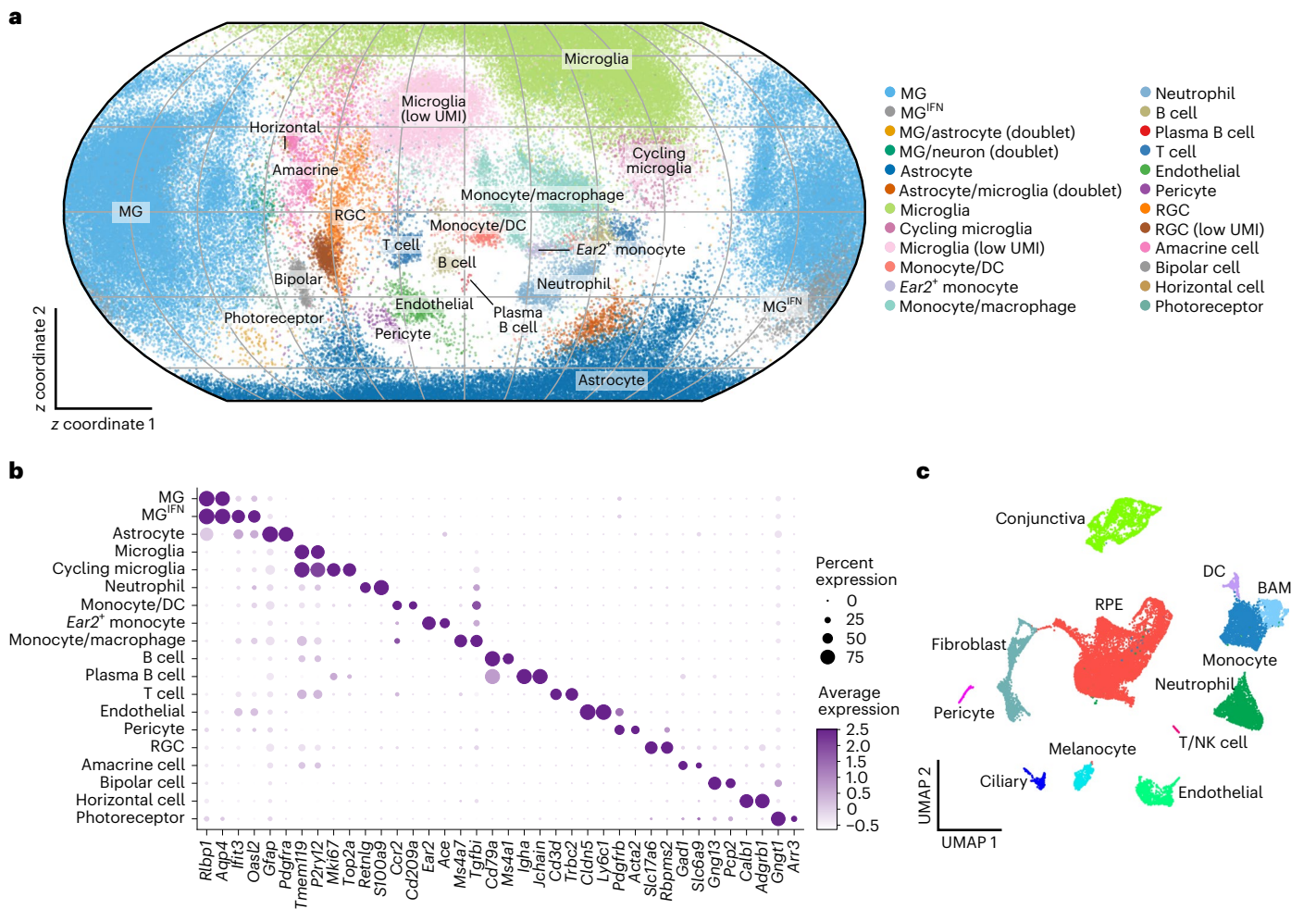


Fig. 1 | A single-cell atlas of the retina tissue ecosystem following ONC.

a, ScPhere embedding of 121,309 single-cell profiles (dots) from the retina at baseline (0 d.p.c.) and at 0.5, 1, 2, 4, 7 and 14 d.p.c., projected to two dimensions (2D) by the Equal Earth map projection method and colored by cell type. **b**, The fraction of expressing cells (dot size) and mean expression in expressing cells

(dot color) of selected marker genes (columns) across 19 cell types identified in the analysis in **a**, including residual neurons (rows). **c**, Two-dimensional UMAP for 21,275 single cells profiled from the mouse posterior eyecup at baseline and at 0.5, 1 and 2 d.p.c. colored by cell type.

(RGCs) are crushed, resulting in ~80% RGC death within ~2 weeks; the surviving RGCs do not regenerate new axons, and visual function is not recovered⁶. Previous single-cell RNA sequencing (scRNA-seq) of RGCs following ONC in mice has characterized 46 RGC subtypes⁷, with marked differences between subtypes in the propensity to survive ONC^{7,8}, and highlighted neuron-intrinsic programs underlying selective resilience and regeneration^{7,9}. Retinal glia and immune cells also impact RGC survival and regeneration^{10–14}, and the retinal pigment epithelium (RPE), which constitutes the outer blood–retinal barrier (oBRB), is a site of immune activity after injury^{15–17}. Deeper characterization of non-neuronal retinal and RPE cells at baseline and after ONC can help elucidate the potential of these cells for healing.

Here, we profiled immune, glial and RPE cells by scRNA-seq in uninjured mouse retinas and at six time points after ONC to study tissue-level dynamics after injury. We characterized cell heterogeneity at baseline and following injury, charting a three-phase response and multicellular inflammatory cascades, providing mechanistic insights and a resource for generating and testing further hypotheses in the retina and the CNS at large.

Results

scRNA-seq captures diverse non-neuronal retinal cells

To generate an scRNA-seq atlas of non-neuronal retinal cells, we profiled CD45⁺ immune cells, GLAST⁺ Müller glia (MG) and CD140a⁺ astrocytes

from the retina, and RPE and immune cells from the eyecup of uninjured mice (day 0 after ONC; 0 d postcrush (d.p.c.)) and of mice with ONC at 0.5, 1, 2, 4, 7 and 14 d.p.c. (retina) and at 0.5, 1 and 2 d.p.c. (eyecup; Extended Data Fig. 1a–f). We recovered 121,309 high-quality retinal single-cell profiles annotated to subsets by differentially expressed marker genes (Fig. 1a,b) and designated 107,067 non-neuronal cells. We used scPhere to integrate the data with time as a batch variable (Fig. 1a and Extended Data Fig. 2a,b) for effective annotation before comparing cells across time (Methods). Marker expression remained sufficiently invariant to annotate 14 major cell subsets (Extended Data Fig. 2c): MG (*Rlbp1* and *Aqp4*), interferon (IFN)-response MG (MG^{IFN}; *Ifit3* and *Oasl2*), astrocytes (*Gfap* and *Pdgfra*), microglia (*Tmem119* and *P2ry12*), cycling microglia (*Mki67* and *Top2a*), neutrophils (*Retnl* and *S100a9*), monocytes/dendritic cells (DCs; *Ccr2* and *Cd209a*), *Ear2*⁺ monocytes (*Ear2* and *Ace*), monocytes/macrophages (*Ms4a7* and *Tgfb1*), B cells (*Cd79a* and *Ms4a1*), plasma B cells (*Igha* and *Jchain*), T cells (*Cd3d* and *Trbc2*), endothelial cells (*Cldn5* and *Ly6c1*) and pericytes (*Pdgfrb* and *Acta2*). We also profiled 21,275 eyecup cells, partitioned them into 12 subsets and annotated them by expression signatures and marker genes (Fig. 1c and Extended Data Fig. 2d,e)^{18,19}. RPE (*Rdh5*, *Rpe65* and *Rlbp1*) and immune cells comprised 42.3% and 30% of cells, respectively, including neutrophils (*Srgn* and *Slpi*), monocytes (*Ccr2* and *Ms4a6c*), border-associated macrophages (BAMs; *Ms4a7* and *Lyz2*), DCs (*Cd74* and *Lsp1*) and T cells/natural killer cells (T/NK cells; *Nkg7* and *Trbc2*).

Other subsets included conjunctival epithelium (*Krt15* and *Gsto1*), scleral fibroblasts (*Dcn* and *Igfbp5*), *Kdr^{hi}* and *Kdr^{lo}* endothelial cells (*Flt1* and *Cldn5*; Extended Data Fig. 2f)²⁰, melanocytes (*Serpina3n* and *Mlana*), ciliary epithelium (*Gpx3* and *Penk*) and pericytes (*Rgs5* and *Mgp*; Fig. 1c and Extended Data Fig. 2e). Overall, the atlas captured diverse non-neuronal retinal and eyecup cells.

Retinal immune cell composition changes following ONC

Analysis of 30,427 *Ptprc⁺* (CD45⁺) retinal immune cells indicated a temporal cascade of compositional changes with three distinct, albeit partly overlapping, stages (Fig. 2a,b and Extended Data Fig. 3a). The first stage (0.5–2 d.p.c.) was defined by a substantial increase in the number of *S100a8⁺S100a9⁺Retnlg⁺* neutrophils (11.7% of immune cells at 1 d.p.c. compared to 1.5% in the uninjured retina) and *Ly6C⁺(Ccr2⁺Ly6c2⁺Chil3⁺Plac8⁺)* monocytes (8.6% at 1 d.p.c. compared to 0.4% in the uninjured retina; Fig. 2b) as well as smaller populations of *Ccr2⁺Ccl5⁺CD209⁺* monocyte-derived DCs with high major histocompatibility complex class II (MHC class II) gene expression (4.8% at 1 d.p.c. compared to 0.1% at 0 d.p.c.) and *Ccr9⁺* plasmacytoid DCs (0.1% at 0 d.p.c. and 1.1% at 1 d.p.c.). A minor subset of *Ly6C⁺(Ear2⁺Nr4a1⁺Trem14⁺)* monocytes, which did not express *Ccr2* or *Ly6c2*, increased to 1.4% at 1 d.p.c. from 0.4% at 0 d.p.c. (Fig. 2b). We validated neutrophil infiltration by Ly6G staining in retinal sections (Extended Data Fig. 3b). In whole-mount retinas from *Ccr2^{RFP/+}* transgenic mice, in which CCR2⁺Ly6C⁺ monocytes can be traced by red fluorescence protein (RFP) expression, CCR2–RFP monocytes were concentrated around the optic nerve head (ONH; the exit point of RGC axons from the retina to the brain) at 1 d.p.c. (Fig. 2c). At 2 d.p.c., these cells were distributed peripherally across the innermost layers of the retina (the nerve fiber layer (NFL), ganglion cell layer (GCL) and inner plexiform layer (IPL)) and acquired an elongated morphology, indicating maturation into macrophages (Fig. 2c and Extended Data Fig. 3c). Some CCR2–RFP cells were closely apposed to SMI32⁺ RGCs and their axons (Fig. 2d).

The intermediate phase, at 2–7 d.p.c., was characterized by microglia proliferation (two clusters of *Mki67⁺* cycling microglia) and the accumulation of three non-microglial macrophage subsets (*Ms4a7⁺* MHC class II^{hi}, *Ms4a7⁺* MHC class II^{lo} and *Gpnmb⁺* macrophages) and *Ccr7⁺* DCs (Fig. 2b). The late phase (7–14 d.p.c.) was characterized by the accumulation of adaptive immune cells, including *Igha⁺Jchain⁺* plasma B cells, *Trbc2⁺Cd3g⁺* T cells and *Gzma⁺Nkg7⁺* NK cells (five to ninefold at 14 d.p.c. compared to uninjured retina). T cells, NK cells and *Cd79a⁺* B cells were also present in the uninjured retina (Fig. 2b), similar to reports in the naive brain^{21,22}. Thus, the cellular response to CNS injury mirrored wound healing in peripheral tissues^{1,2}.

Because RGCs generally fail to regenerate (unlike wound healing), we assessed cellular and intercellular events in the retina and eyecup that could drive the inflammatory cascade and its impact on RGCs. To assess whether the increase in immune cells observed between 0.5 and 2 d.p.c. was due to infiltration through the oBRB, we analyzed 6,415 immune cell profiles from the eyecup of uninjured

and ONC mice. BAMs, which expressed *Aif1*, *Csf1r*, *Cd68*, *Ms4a7*, *Mrc1* (encoding CD206), *Pf4* and *Stab1*, were the predominant immune cell subset in the uninjured eyecup (Fig. 2e) and ranged in expression of several genes associated with MHC class II^{hi} and MHC class II^{lo} BAMs in other CNS compartments^{23,24} (Fig. 2f). We validated the presence of *Ms4a7⁺* and MHC class II⁺CD206⁺ BAMs in sections of uninjured eyecup (Fig. 2g and Extended Data Fig. 3d). Similar to the retina, we observed a transient increase in *S100a8⁺S100a9⁺Retnlg⁺* neutrophils at 0.5 d.p.c. and a proportional decrease in BAMs, followed by an increase in *Ccr2⁺Ly6c2⁺Chil3⁺* monocytes at 1–2 d.p.c. (Fig. 2e,h). The relative reduction in BAMs was likely due to increased monocytes and neutrophils, as absolute BAM numbers were comparable to those observed in uninjured control eyecups (Fig. 2g and Extended Data Fig. 3e). Immunohistochemical (IHC) staining in whole-mount eyecups from *Ccr2^{RFP/+}* mice indicated that most CCR2–RFP cells were posterior to the RPE in the naive eye (Extended Data Fig. 3f) and likely represented choroidal short-lived monocyte-derived macrophages¹⁶, while at 1–2 d.p.c., CCR2–RFP cells were associated with the RPE¹⁵ (Fig. 2h and Extended Data Fig. 3g) and mostly concentrated around the ONH (Fig. 2i). Together, with center-to-periphery spreading of CCR2–RFP monocytes across the GCL, this indicated that the ONH was the predominant site of leukocyte infiltration into the retina. Interactions between chemokines and their receptors were enriched between BAMs, neutrophils and monocytes throughout the time course (Fig. 2j,k and Methods). Thus, immune cell composition was dynamically remodeled across the retina following ONC, with a likely role for eyecup-resident macrophages in peripheral immune infiltration.

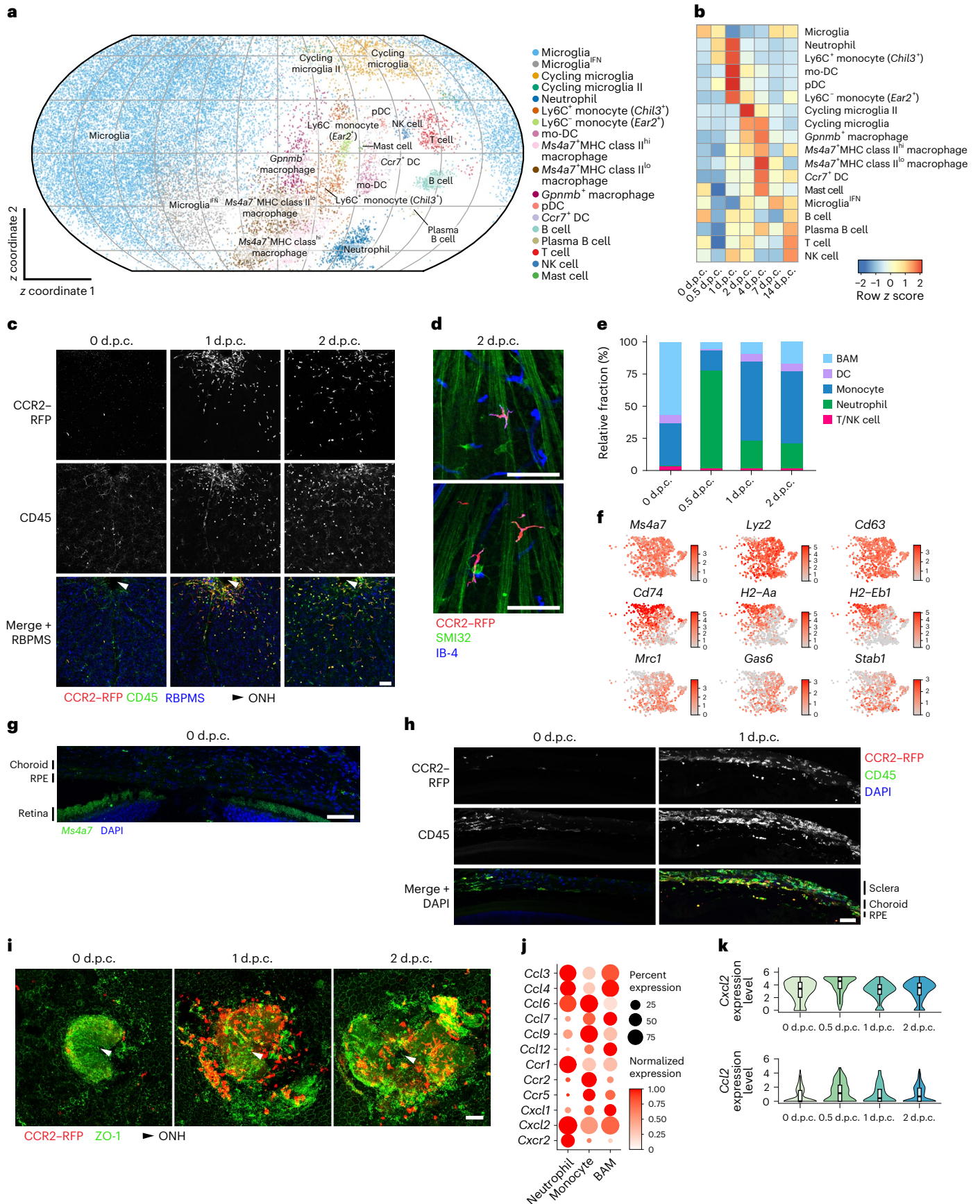
Glia reactivation includes cues for immune infiltration

To gain insight into retinal cues that drive the progression of the inflammatory response, we analyzed resident MG, astrocytes and microglia. *Rlbpl1⁺Aqp4⁺Glul⁺* MG (Extended Data Fig. 4a; ~3% of naive retina cells) span the retina's entire thickness and contact all neuronal layers²⁵, while *Pdgfra⁺S100b⁺Gfap⁺* astrocytes (Extended Data Fig. 4a; ~0.2% of retinal cells) reside in the GCL and NFL in tight contact with the inner retina blood vessels²⁵. Microglia (~0.5% of naive retina cells) showed decreased expression of signature genes (for example, *P2ry12* and *Tmem119*) from 0.5 d.p.c. (Extended Data Fig. 4b) and increased proliferation at 2–4 d.p.c. (Fig. 3a,b), consistent with responses to other CNS insults^{16,26–30}. At 4 d.p.c., cycling *Ki67⁺* microglia were localized in the GCL, IPL and outer plexiform layer (OPL) in situ (Fig. 3c and Extended Data Fig. 4c,d). There was a moderate increase in a microglia subset that expressed IFN-stimulated genes (ISGs; for example, *Ifit3*, *Isg15* and *Irf7*), which we termed IFN-response microglia (microglia^{IFN}), also detected in the naive retina (10.5% at 7 d.p.c. compared to 8.1% at 0 d.p.c.; Fig. 3a,b).

MG profiles formed an expression continuum (Fig. 3d,e). A small subset of MG^{IFN}-expressed ISGs, such as *Ifit3*, *Isg15* and *Bst2* (Fig. 3e), increased in frequency (3.6% of all MG at 1 d.p.c. compared to 1.9% in naive retinas) and peaked at 4 d.p.c. (8.4%; Fig. 3f). Reactive MG^{25,31} had higher expression of *Gfap* and *Vim* (encoding intermediate filaments)

Fig. 2 | A temporal inflammatory cascade of infiltrating leukocytes and expanding resident macrophages after ONC. **a**, SPhere embedding of 30,427 immune cell profiles (dots) from the retina at 0, 0.5, 1, 2, 4, 7 and 14 d.p.c., projected to 2D by the Equal Earth map projection method and colored by cell type. **b**, Row z scores showing the changes in relative abundance of each immune cell subset across time; mo-DC, monocyte-derived DCs; pDC, plasmacytoid DCs. **c,d**, Representative images of IHC on retina whole mounts from *Ccr2^{RFP/+}* mice showing CCR2–RFP monocytes (red) in the retinal GCL (RBPMs, blue) at 1–2 d.p.c. (**c**) and at 2 d.p.c. among SMI32⁺ RGC somas and axons (**d**; green). GS-IB-4 isolectin (blue) labels blood vessels and activated monocytes/macrophages ($n = 2–3$ mice per time point per experiment; data are representative of two independent experiments). **e**, Fraction (y axis) of immune cell subsets isolated from the eyecup at 0, 0.5, 1 and 2 d.p.c. (x axis). **f**, Feature plots of BAMs in the eyecup colored by expression of pan- (top), MHC class

II^{hi}- (middle) and MHC class II^{lo}- (bottom) BAM genes²³. **g**, Representative image of smFISH for *Ms4a7* (green) in naive (0 d.p.c.) mouse eyecup ($n = 3$ mice). **h,i**, Representative images of IHC on eyecup sections (**h**) or whole mounts (**i**) from *Ccr2^{RFP/+}* mice, showing CCR2–RFP monocytes (red) in the eyecup at 0, 1 and 2 d.p.c. ($n = 2$ mice per time point; data are representative of three independent experiments). **j**, Fraction of expressing cells (dot size) and normalized expression level (dot color) of chemokines and their receptors (rows) by BAMs, neutrophils and monocytes (columns) in the eyecup at 0, 0.5, 1 and 2 d.p.c. **k**, Distribution of expression of *Cxcl2* and *Ccl2* by eyecup BAMs over time (0 d.p.c., $n = 215$ cells; 0.5 d.p.c., $n = 115$; 1 d.p.c., $n = 99$; 2 d.p.c., $n = 473$). Box plots denote the medians and the interquartile ranges (IQRs). The whiskers of a box plot are the lowest datum still within 1.5× the IQR of the lower quartile and the highest datum still within 1.5× the IQR of the upper quartile; scale bars, 50 μm.



and lower expression of the MG markers *Slc1a3*, *Rlbp1* and *Glul* (Fig. 3e). Reactive MG were most prevalent at 0.5 d.p.c. (13.3% of all MG compared to 0.26% in naive retinas; Fig. 3f) and expressed high levels of excitotoxin- and light injury-induced genes³¹ (for example, *Nfkb1*, *Bmp1* and *Hmga1*; Extended Data Fig. 4e), suggesting induction of programs common across various retinal injury models.

Astrocytes included reactive astrocytes that expressed *Lcn2*, *Chil1* and *Cp* (Fig. 3g,h), recapitulating expression programs from CNS injury and disease models^{32–36}. Reactive astrocytes increased at 0.5 d.p.c. (25.4% of astrocytes compared to 0.9% at baseline) and gradually decreased from 1 d.p.c. (Fig. 3i). From 0.5 d.p.c. to 14 d.p.c., compared to 0 d.p.c., all astrocytes increased the expression of a pan-reactive astrocyte signature of genes known to be upregulated after ischemic stroke and lipopolysaccharide (LPS)-induced neuroinflammation^{34,35}, with higher expression of these genes in reactive astrocytes (Extended Data Fig. 4f). Rare cycling astrocytes (~0.3% of all astrocytes) expressed cell cycle genes and neural progenitor markers (*Nes* and *Fabp7*) at 2–4 d.p.c. (Fig. 3h–j)³⁷. The proportion of *Igf2*⁺ astrocytes decreased at 0.5 d.p.c. (22.2% compared to 45.9% at 0 d.p.c.; Fig. 3i). *Igf2*⁺ astrocytes expressed the highest levels of angiogenesis factors *Igf2*, *Angpt4* and *Vegfa* (Fig. 3h), possibly reflecting interactions with blood vessels. ISG-expressing (*Ifit1*, *Ifit3* and *Isg15*) astrocytes (Astro^{IFN}; Fig. 3h) represented a small subset, and their frequency doubled at 4 d.p.c. (4.3% versus 2% at 0 d.p.c.; Fig. 3i). From 0.5 d.p.c., all astrocytes increased the expression of a disease-associated astrocyte gene signature characterized in Alzheimer's disease³², including *Ctsb*, *Vim*, *Osmr*, *Serpina3n*, *Gsn* and *Ggta1* (Fig. 3k). A classifier trained on our astrocyte profiles predicted the presence of the ONC-reactive subset after systemic inflammation with LPS³³ (Fig. 3l and Extended Data Fig. 4g,h), indicating that shared expression programs are activated in astrocytes across CNS pathologies. We further analyzed the expression of glial metal metabolism and microglia-to-astrocyte signaling genes (Supplementary Notes 1 and 2). Thus, glial reactivation started early after injury, before substantial RGC loss⁷.

Astrocytes and microglia mediate immune cell recruitment into the CNS by cytokine secretion^{3,38}. Retinal astrocytes and microglia upregulated the expression of neutrophil and monocyte chemoattractants at 0.5 d.p.c. (Fig. 3m), coinciding with the emergence of neutrophils and monocytes in the retina. Single-molecule fluorescence in situ hybridization (smFISH) in retinal sections confirmed *Ccl2* expression by *Gfap*⁺ astrocytes at 0.5 d.p.c. (Fig. 3n), suggesting that astrocyte and microglia reactivation might connect injured RGCs and peripheral immune cells to facilitate the immune response.

A unique RPE cell state emerges early after ONC

To identify other early events, we partitioned the RPE cells into five subsets by differentially expressed genes (Fig. 4a,b and Extended Data Fig. 5a). C0 and C2 were similar (*Rdh5*, *Trf* and *Rgr*) except for higher expression of melanin production genes in C0 (Fig. 4b). C15 was

enriched for heat shock protein and immediate early genes (*Hspa1a*, *Fos* and *Jun*; Fig. 4b). C4 was enriched for development-related genes, such as *Abhd2* (spermatogenesis regulator), *Notch2* (embryonic brain and retina development) and *Spry2* (lens development; Fig. 4b and Supplementary Note 3). C0, C2, C4 and C15 frequencies were similar before and after ONC, but C12 was enriched at 0.5, 1 and 2 d.p.c. (12.1%, 16.8% and 7.12% of RPE cells, respectively, versus 2% at baseline; Fig. 4c).

C12 cells expressed high levels of genes associated with injury and cell stress (for example, *Tnfrsf12a*, *Serpina3n* and *Gpnmb*) and epithelial-to-mesenchymal transition (for example, *Vim*, encoding vimentin, *Acta2*, *Lgals1* and *Lgals3*; Fig. 4b,d). We validated *Tnfrsf12a* and vimentin upregulation in eyecup sections after crush by smFISH and IHC (Fig. 4e,f). Some C12 genes were upregulated after ONC in all RPE cells (Extended Data Fig. 5b), including *Vim*, *Gpnmb* and *Plin2*, a lipid droplet binding protein with roles in the visual cycle and in innate immunity³⁹ (Extended Data Fig. 5c). We validated increased PLIN2 protein expression at 0.5 d.p.c. in RPE whole mounts (Fig. 4g). Expression changes in all RPE cells after ONC included decreased expression of the circadian gene *Dbp* and increased expression at 2 d.p.c. of *Nog*, which encodes the bone morphogenic protein antagonist Noggin, which is involved in RPE differentiation⁴⁰ (Extended Data Fig. 5b,d,e). Thus, expression changes in the RPE after ONC reflected stress-related processes, such as epithelial-to-mesenchymal transition and dedifferentiation⁴¹.

Receptor–ligand (RL) interactions between RPE, BAMs, neutrophils and monocytes increased in the eyecup after ONC (Fig. 4h), suggesting an integrated response at 0.5–1 d.p.c. (Fig. 4i). For instance, eyecup myeloid cells expressed *Osm* (encoding oncostatin M), a cytokine that is neuroprotective in the retina⁴², while RPE cells upregulated its receptor, *Osmr*, at 0.5 d.p.c. (Fig. 4i and Extended Data Fig. 5b). Most (82.8%) genes of the top 20 RL pairs at 0.5–1 d.p.c. were differentially expressed in C12 compared to other RPE clusters. Among those, RL pairs uniquely expressed after ONC included *Rbp4–Stra6* (retinol transport), *Trf–Tfrc* (metal metabolism) and *Tnc–Itgav* (retinal and optic nerve pathology⁴³; Fig. 4j). Thus, the retinal response to ONC extends to the outer retina, with a potential role for C12 RPE cells in remodeling the injured RPE microenvironment.

Distinct macrophage subsets increase in the retina after ONC

During the intermediate phase of the inflammatory cascade, three subsets of non-microglial macrophages, expressing markers of peripherally derived macrophages and BAMs^{23,24,44} (for example, *Ms4a7*, *Lyz2* and *ApoE*; Fig. 5a), peaked at 4 d.p.c. (Extended Data Fig. 6a). *Ms4a7*⁺ MHC class II^{hi} and *Ms4a7*⁺ MHC class II^{lo} subsets (Fig. 5a) mirrored the MHC class II^{hi} and MHC class II^{lo} BAM subsets in the homeostatic brain and spinal cord^{23,24} (Extended Data Fig. 6b). The frequency of *Ms4a7*⁺ MHC class II^{hi} and *Ms4a7*⁺ MHC class II^{lo} cells among all immune cells increased 1.9- and 3-fold, respectively, compared to 0 d.p.c. (Extended Data Fig. 6a). *Gpnmb*⁺ macrophages increased 12.9-fold from 0 to 4 d.p.c. and

Fig. 3 | Early reactivation of retinal glia and microglia following ONC.

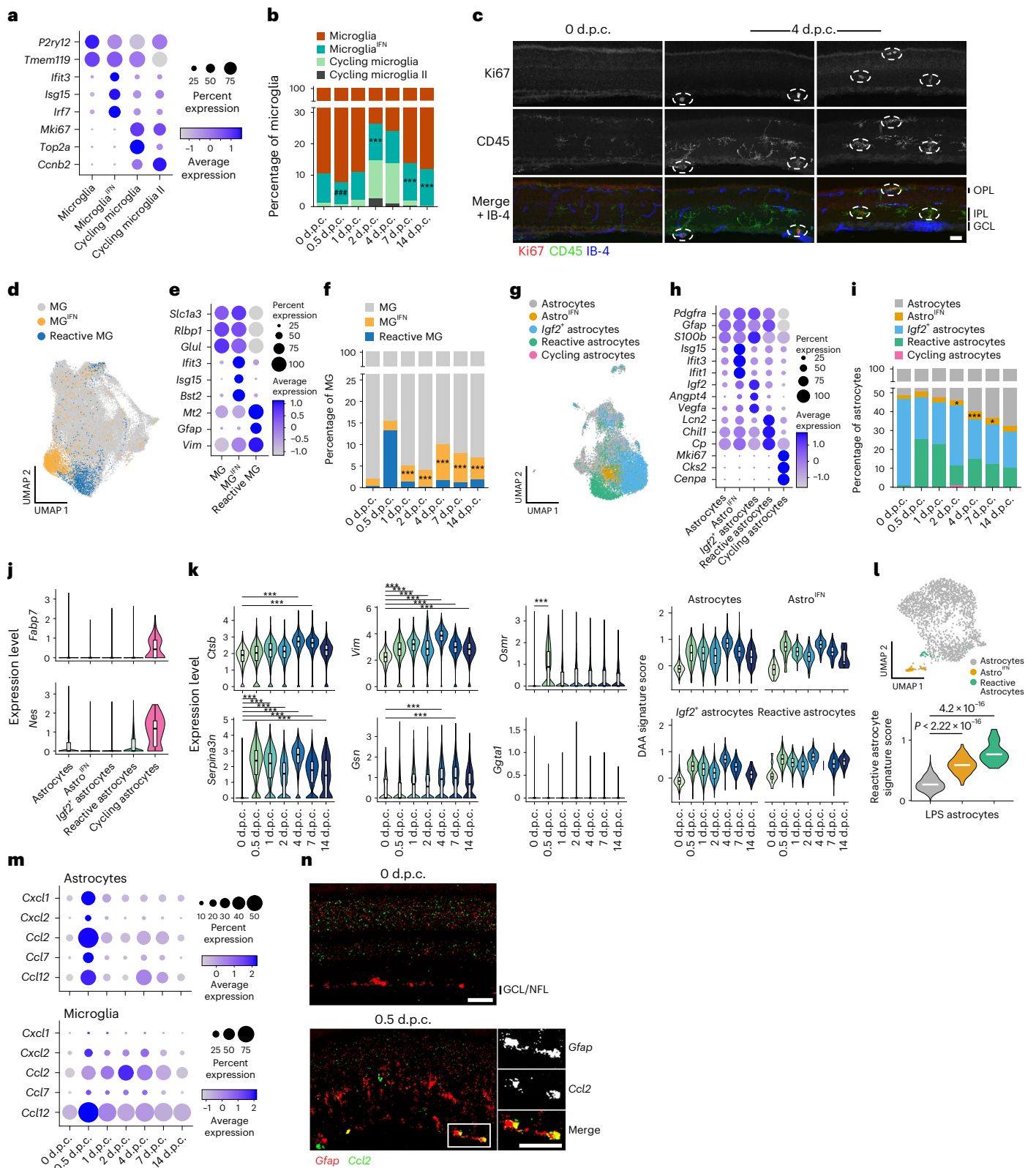
a,e,h, Fractions of cells (dot size) in each microglia (**a**), MG (**e**) and astrocyte (**h**) subset and mean expression level in expressing cells (dot color) of genes differentially expressed between subsets. **b,f,i**, Fractions of microglia (**b**), MG (**f**) and astrocyte (**i**) subsets at 0, 0.5, 1, 2, 4, 7 and 14 d.p.c. Asterisks (hashes) indicate increases (decreases) in the microglia^{IFN} (**b**), MG^{IFN} (**f**) or Astro^{IFN} (**i**) subsets relative to 0 d.p.c.; **P* < 0.05, ****P* < 0.001 (Fisher's exact test, two sided); Benjamini–Hochberg-adjusted *P* values). **c**, Representative IHC images of retinal sections at 0 and 4 d.p.c. showing Ki67⁺ (red) and CD45⁺ (green) microglia (*n* = 3 mice per time point). The dashed circles depict Ki67⁺CD45⁺ cells. **d,g**, UMAP of 54,565 MG (**d**) and 18,959 astrocytes (**g**) from 0, 0.5, 1, 2, 4, 7 and 14 d.p.c. colored by subset. **j**, Distribution of *Fabp7* and *Nes* expression across astrocyte subsets (astrocytes, *n* = 10,733 cells; Astro^{IFN}, *n* = 597; *Igf2*⁺ astrocytes, *n* = 4,945; reactive astrocytes, *n* = 2,625; cycling astrocytes, *n* = 59). **k**, Distribution of the expression of disease-associated astrocyte (DAA)³² genes (left) in

astrocytes at 0 d.p.c. (*n* = 1,968), 0.5 d.p.c. (*n* = 1,179), 1 d.p.c. (*n* = 3,384), 2 d.p.c. (*n* = 4,209), 4 d.p.c. (*n* = 4,453), 7 d.p.c. (*n* = 3,223) and 14 d.p.c. (*n* = 543) and as a signature score across astrocyte subsets (right). Box plots denote medians and IQRs; whiskers are the lowest datum still within 1.5× the IQR of the lower quartile and the highest datum still within 1.5× the IQR of the upper quartile; ****P* < 0.001 and fold change of >1.5 over 0 d.p.c. (logistic regression likelihood ratio test with Benjamini–Hochberg correction for multiple comparisons). **l**, Top, UMAP of astrocytes from LPS-induced inflammation³³ colored by ONC astrocyte subset. Bottom, distribution of reactive astrocyte signature score across astrocytes from LPS-induced inflammation³³ classified to ONC astrocyte subsets (Student's *t*-test, one sided). **m**, Dot plot showing the expression of chemokine genes by astrocytes (top) and microglia (bottom) at 0, 0.5, 1, 2, 4, 7 and 14 d.p.c. **n**, Representative smFISH images of retinal sections at 0 and 0.5 d.p.c. for *Ccl2* (green) and *Gfap* (red; *n* = 3 mice per time point); scale bars, 50 μm.

expressed high levels of *Gpnmb*, *Fabp5*, *Spp1* and *Lgals3* (Fig. 5a), reminiscent of disease-associated microglia (DAM)^{28,29} and lipid-associated macrophages from various human tissues^{45,46}. *Gpnmb*^{hi}*Ptprc*⁺ immune cells expressing *Ms4a7* were detected in the inner retina at 7 d.p.c. by smFISH (Extended Data Fig. 6c). Analysis of data from chronic lesions from individuals with multiple sclerosis⁴⁷ demonstrated a cell subset with an overlapping profile (*GPNUMB*, *LGALS3*, *LPL* and *CD68*; Extended Data Fig. 6d), also reported in retinas from individuals with

glaucoma and in glaucoma mouse models⁴⁸. This signature also overlapped with RPE C12 cells (Extended Data Fig. 6e), suggesting a shared injury-induced program across cell types with potentially overlapping functions.

We localized *Ms4a7*^{hi} MHC class II^{hi} and *Ms4a7*^{lo} MHC class II^{lo} macrophages in retinal whole mounts by combined smFISH and IHC. In naive retina, ramified IA-IE⁺ (MHC class II⁺) cells near the ONH and at the retinal margins adjacent to the ciliary body^{49,50} (Extended Data



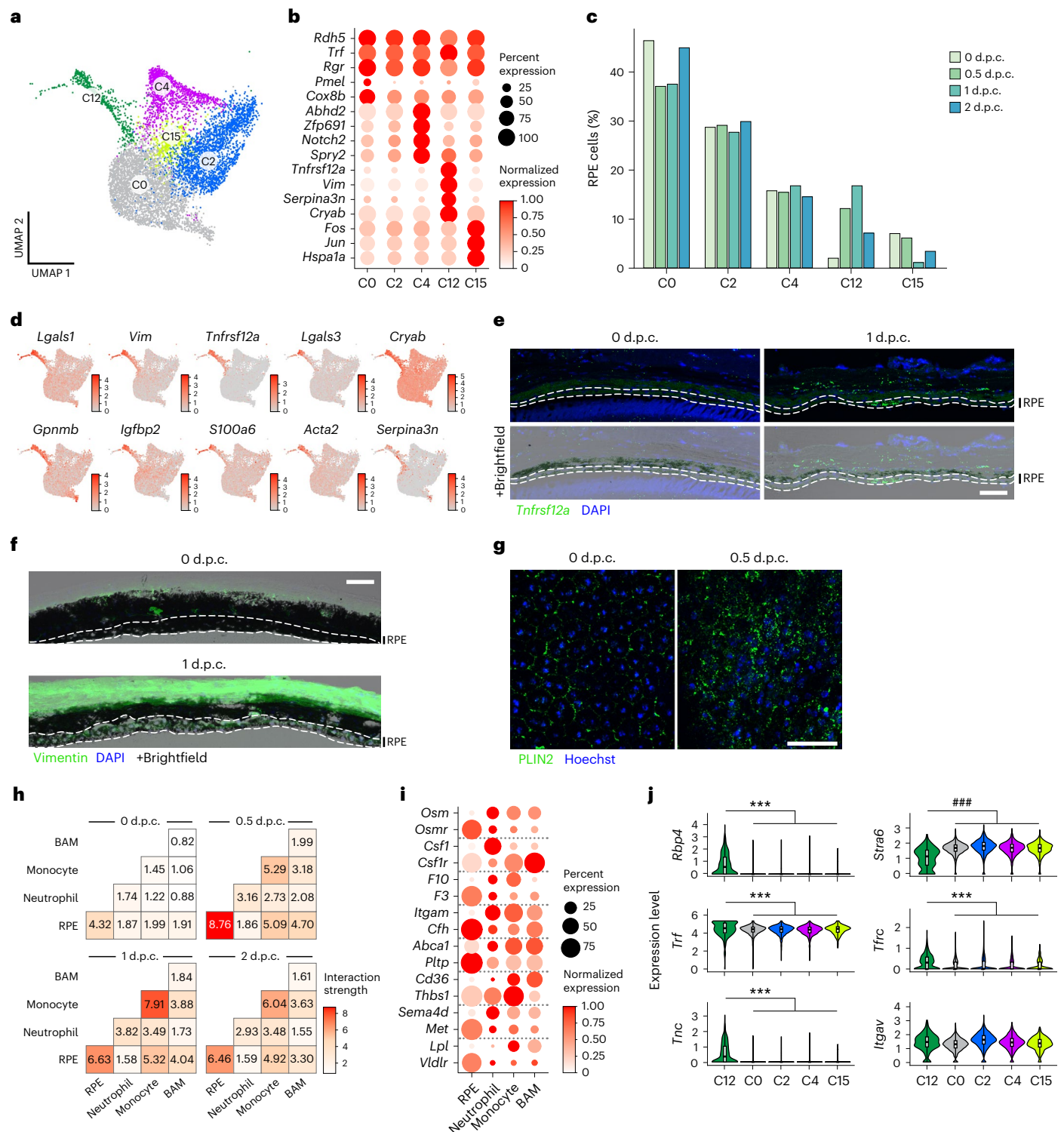


Fig. 4 | A unique RPE cell state emerges early after ONC. a, UMAP for 8,013 RPE cells colored by subset (cluster). **b**, Fraction of expressing cells (dot size) and normalized expression in expressing cells (dot color) of differentially expressed genes (rows) between RPE clusters (columns). **c**, RPE cluster proportion changes. Shown are cell frequencies (y axis) of RPE clusters (x axis) out of all RPE cells at 0, 0.5, 1 and 2 d.p.c. **d**, Feature plots of RPE cells colored by expression of C12 top differentially expressed genes. **e–g**, Representative smFISH image of *Tnfrsf12a* (green; **e**) and IHC images of VIM (green) at 0 and 1 d.p.c. (**f**) and PLIN2 (green) at 0 and 0.5 d.p.c. (**g**; $n = 3$ mice per time point); scale bars, 50 μm . **h**, Changes in interaction strength between pairs of cells from the eyecup over time. **i**, Fraction of expressing cells (dot size) and normalized expression level (dot color) of

ligands and their cognate receptors (rows) by RPE, neutrophils, monocytes and BAMs (columns) in the eyecup. Shown are interactions enriched at 0.5–1 d.p.c. **j**, Unique interactions between RPE C12 and the other RPE cells. Shown are distributions of the expression of genes encoding ligands and their cognate receptors by RPE subsets (C12, $n = 586$; C0, $n = 3,459$; C2, $n = 2,340$; C4, $n = 1,228$; C15, $n = 400$); ***/### $P < 0.001$ denotes increased/decreased expression in C12 compared to the other RPE clusters (logistic regression likelihood ratio test; P values adjusted with the Benjamini–Hochberg method for multiple comparisons). Box plots denote medians and IQRs; whiskers are the lowest datum still within 1.5 \times the IQR of the lower quartile and the highest datum still within 1.5 \times the IQR of the upper quartile.

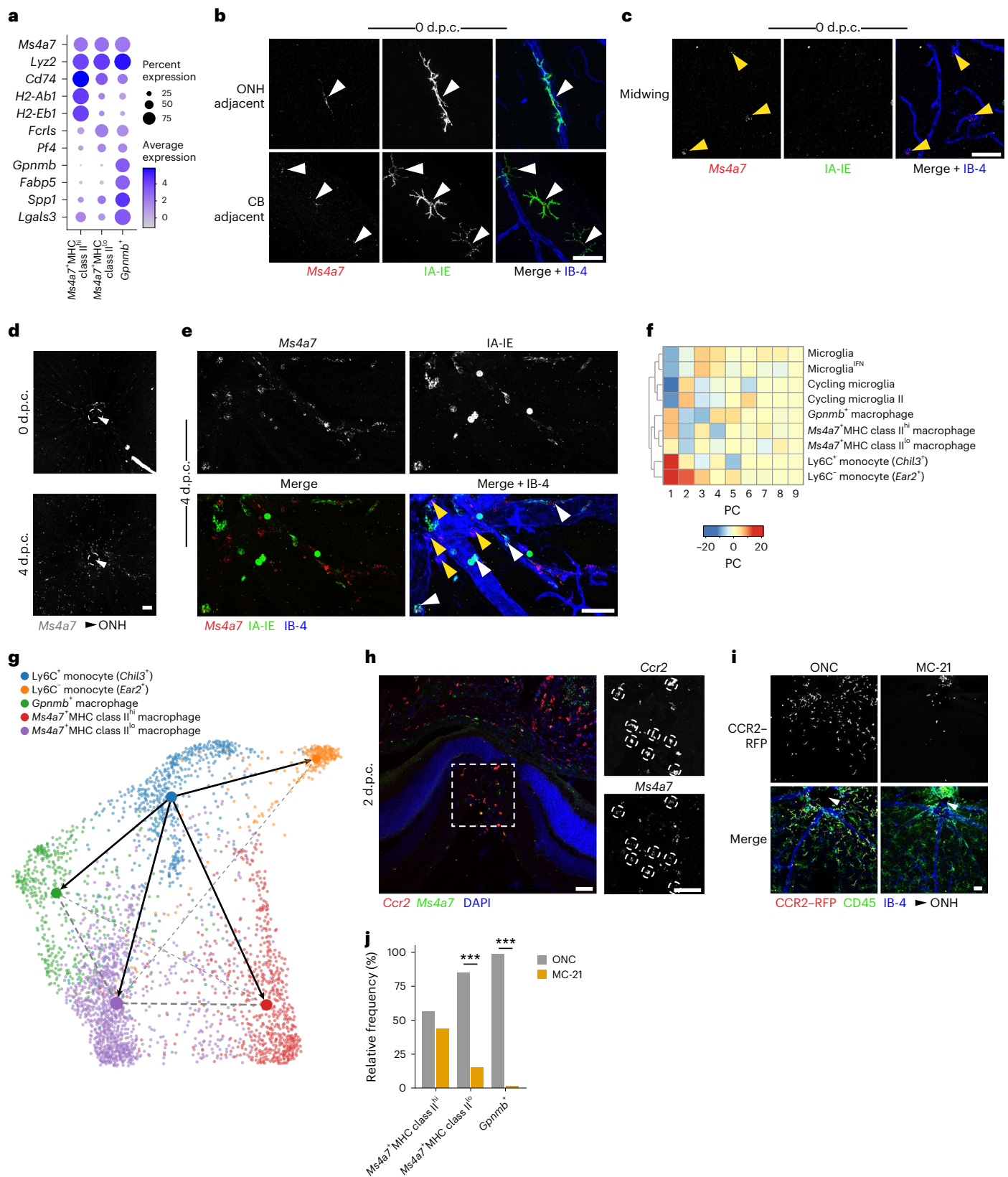


Fig. 6f) expressed *Ms4a7* (Fig. 5b). Conversely, *Ms4a7*⁺IB-4⁺IA-IE⁻ cells, likely corresponding to *Ms4a7*⁺MHC class II^{lo} cells, were amoeboid and dispersed across the inner retinal surface (Fig. 5c). Thus, *Ms4a7*⁺ resident retinal macrophages included perivascular and ciliary body-adjacent MHC class II^{hi} populations^{49,50} and an additional, previously undescribed, MHC class II^{lo} subset. More *Ms4a7*⁺ cells were

present around the ONH at 4 d.p.c. than at 0 d.p.c. (Fig. 5d), including both *Ms4a7*⁺IA-IE⁺ and *Ms4a7*⁺IA-IE⁻ cells (Fig. 5e).

Because *Ms4a7*⁺ and *Gpnmb*⁺ macrophage subsets had profiles more similar to monocytes than to microglia (for example, *Ms4a6c*, *Tgfb1* and *Ifitm3*; Fig. 5f), we tested whether they originated from infiltrating monocytes at 0.5–2 d.p.c. Trajectory and RNA velocity analyses

Fig. 5 | Infiltrating monocytes give rise to macrophage subsets in the injured retina with overlapping expression programs to non-microglial resident retinal macrophages. **a**, Fraction of expressing cells (dot size) and mean expression level in expressing cells (dot color) of genes (rows) differentially expressed between *Ms4a7*⁺ MHC class II^{hi}, *Ms4a7*⁺ MHC class II^{lo} and *Gpnmb*⁺ macrophage subsets. **b, c**, Representative images of combined smFISH and IHC on retinal whole mounts from uninjured (0 d.p.c.) retina, showing *Ms4a7* expression (red) in IA-IE⁺ cells (green), around blood vessels (IB-4, blue) and at the marginal retina bordering the ciliary body (**b**) and *Ms4a7* (red) expression in IA-IE⁺ IB-4⁺ cells (yellow arrowheads) across the GCL (**c**; representative of three independent experiments with $n = 1-2$ mice each); CB, ciliary body. The white arrowheads in panel **b** depict *Ms4a7*⁺ IA-IE⁺ cells. **d, e**, Representative smFISH and IHC images of whole-mount retinas from 0 and 4 d.p.c. retinas showing *Ms4a7*⁺ (gray) cells (**d**), including *Ms4a7*⁺ IA-IE⁺ (white arrowheads) and *Ms4a7*⁺ IA-IE⁻ (yellow arrowheads) cells (**e**). A zoomed-in inset from the 4 d.p.c. image in **d** is shown in **e** ($n = 2-3$ mice per time point; data are representative of three

independent experiments). **f**, Cluster analysis showing transcriptional proximity of mononuclear phagocyte subsets in the retina; PC, principal component. **g**, Force-directed layout view of monocyte and macrophage subsets with predicted cell transition vectors (arrows) based on partition-based graph abstraction colored by cell type. **h, i**, Representative images of smFISH on retinal sections at 2 d.p.c. for *Ccr2* (red) and *Ms4a7* (green; **h**) and of IHC of retinal whole mounts from MC-21-treated or untreated mice at 2 d.p.c. (**i**) for CD45 (green), IB-4 (blue) and CCR2-RFP (red; $n = 3$ mice per condition). The dashed square in panel **h** marks the inset shown on the right. The dashed circles depict *Ccr2*⁺ *Ms4a7*⁺ cells. **j**, Relative frequency of *Ms4a7*⁺ MHC class II^{hi}, *Ms4a7*⁺ MHC class II^{lo} and *Gpnmb*⁺ macrophage subsets in the retina at 7 d.p.c. with and without MC-21 treatment (pool of $n = 5$ mice per condition; $n = 4,633/1,551$ and $2,810/96$ single immune cells/macrophages from ONC and MC-21, respectively); *** $P < 0.001$ (Fisher's exact test, two sided; P values adjusted with the Benjamini-Hochberg method for multiple comparisons); scale bars, 50 μ m.

predicted that Ly6C⁺ monocytes gave rise to Ly6C⁻ monocytes (as in fate-mapping studies⁵¹) and also branched into *Ms4a7*⁺ and *Gpnmb*⁺ macrophages (Fig. 5g). An independent optimal transport analysis also indicated Ly6C⁺ monocytes as the probable precursors of these macrophages (Extended Data Fig. 6g). smFISH showed *Ccr2*⁺ *Ms4a7*⁺ double-positive cells in the retina at 2 d.p.c. (Fig. 5h). To experimentally test whether infiltrating CCR2⁺ monocytes give rise to *Ms4a7*⁺ macrophages after ONC, we depleted circulating CCR2⁺ monocytes during the first week after ONC using systemic administration of MC-21, an antibody to CCR2. MC-21 treatment efficiently depleted retinal monocytes (Fig. 5i) and reduced the frequency of *Ms4a7*⁺ and *Gpnmb*⁺ macrophage subsets at 7 d.p.c., as assessed by scRNA-seq (Fig. 5j). This suggested that infiltrating CCR2⁺ monocytes contributed to the increase in those macrophages after injury. Thus, the naive retina harbors distinct subsets of resident macrophages, which are supplemented through monocyte infiltration after injury.

A coordinated IFN response is activated in the injured retina

Next, we characterized microglia^{IFN}, MG^{IFN} and Astro^{IFN}, all of which increased in frequency at the intermediate phase. Microglia expressing an IFN signature are associated with aging and neurodegeneration and have only rarely been identified in the naive adult CNS^{16,26,52,53}. IFIT3⁺ myeloid cells were detected in the GCL, IPL and OPL of uninjured retinas (Fig. 6a). RNA velocity analysis supported a model where cycling microglia transitioned through the microglia^{IFN} state during maturation (Fig. 6b). Retinal Ki67⁺ cells at 4 d.p.c. expressed IFIT3 protein as assessed by IHC (Fig. 6c), consistent with reports of microglia repopulation after depletion in the adult brain⁵⁴. Thirty-seven ISGs that were differentially expressed in microglia^{IFN} (for example, *lfit3*, *lsg15* and *lfitm3*) were also upregulated in brain-repopulating microglia compared to microglia from untreated brain from a separate study⁵⁵ (Extended Data Fig. 7a). These observations suggest that an IFN-response program

activated during microglia self-renewal in the retina after ONC may similarly be activated in the brain as a transitional state toward maturation.

The presence of IFN-response glia in the uninjured retina and their expansion after ONC suggest that these subsets are poised to respond to immune challenge. Supporting this, *Ccl2* expression at 0.5 d.p.c. was higher in microglia^{IFN} and Astro^{IFN} than in the other microglia and astrocyte subsets (Fig. 6d). Expression of some ISGs (for example, *lfit3*) increased in all astrocytes and MG 4-14 d.p.c. (Fig. 6e and Extended Data Fig. 7b), indicating IFN-response propagation. IHC confirmed increased IFIT3 expression in GFAP⁺ astrocytes and MG at 7 d.p.c. compared to 0 d.p.c. (Fig. 6f). A type I IFN response is upregulated in astrocytes during experimental autoimmune encephalomyelitis⁵⁶, and rare subsets of astrocytes expressing an ISG signature are found in the brain and spinal cord across models of pathology³³. Classifiers trained on our data identified an Astro^{IFN} subset in mice treated with LPS³³, congruent with the IFN-response cluster (cluster 8) of that study (Fig. 6g and Extended Data Fig. 7c).

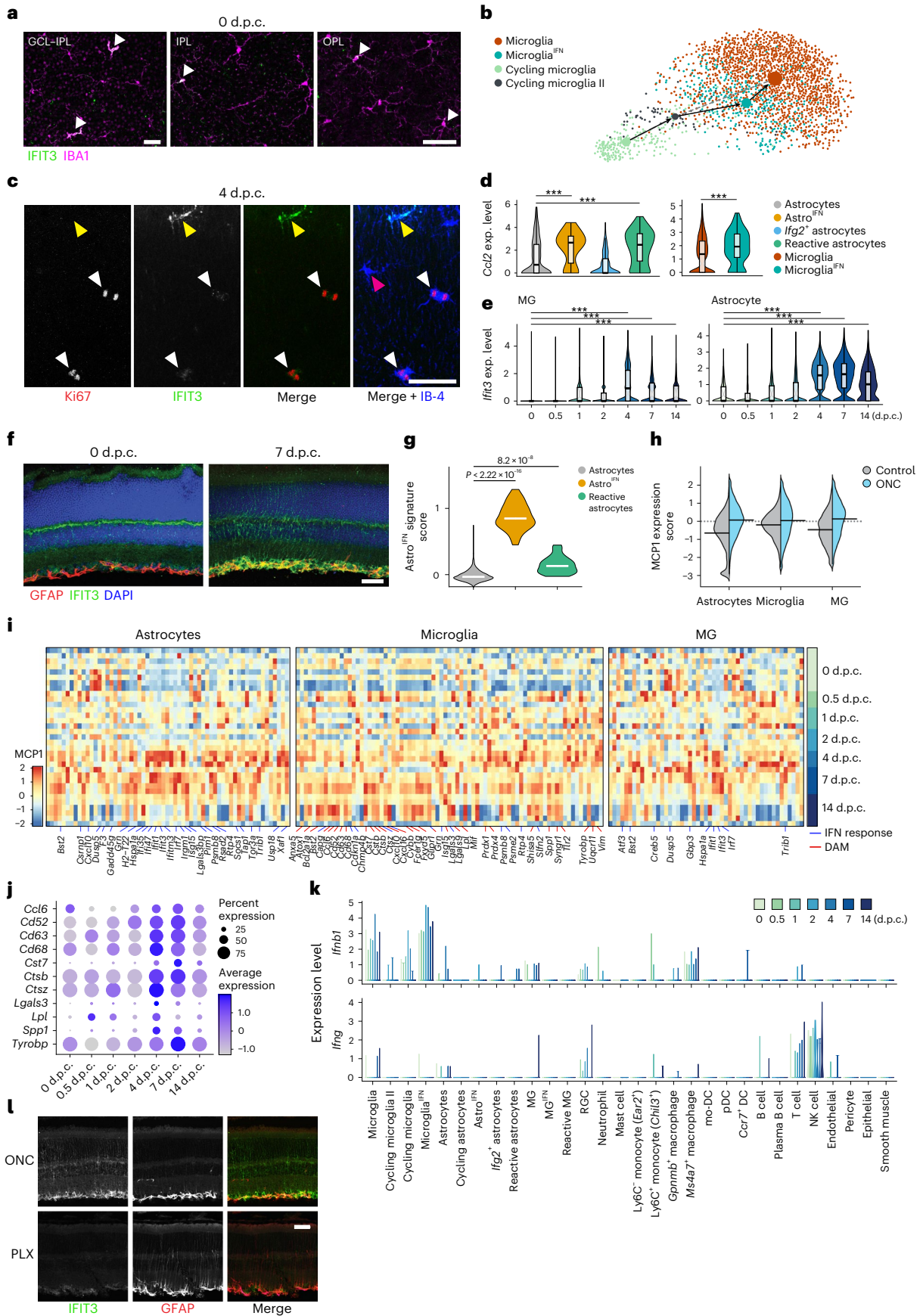
We tested whether the IFN response after ONC was coordinated across astrocytes, microglia and MG using DIALOGUE to identify multicellular gene programs (MCPs) whose expression was co-regulated in these subsets across the retinal dataset (Methods). The top MCP induced in ONC compared to 0 d.p.c. (MCP1; peak, 4-7 d.p.c.; Fig. 6h and Extended Data Fig. 7d,e) was an IFN-response program (37 of 149 MCP genes were IFN-response genes⁵⁷; Fig. 6i and Supplementary Table 1). The microglia component was enriched for DAM genes (30 of 149 MCP genes were DAM genes^{16,28,29}; Fig. 6i,j and Supplementary Table 1).

To identify potential cellular sources of IFN that could activate the MCP, we analyzed the expression of *lfn* transcripts in the atlas. *lfnb1* was mainly expressed by microglia (including microglia^{IFN}), and by astrocytes, MG, RGCs and *Ms4a7*⁺ macrophages (Fig. 6k). *lfn* was mostly expressed by T and NK cells (Fig. 6k). Retinas from mice treated with PLX5622, a CSF1R inhibitor that depletes microglia and other

Fig. 6 | The IFN response is coordinated in the retina after ONC.

a, c, Representative IHC images on retinal whole mounts showing IFIT3⁺ (green) microglia (IBA1; magenta, white arrowheads) in the naive (0 d.p.c.) retina at the GCL, IPL and OPL (**a**) and Ki67⁺ IFIT3⁺ IBA1⁺ microglia (white arrowheads) at 4 d.p.c. (**c**). The yellow and magenta arrowheads depict IFIT3⁺ Ki67⁺ IBA1⁺ and IFIT3⁺ Ki67⁻ IBA1⁺ microglial cells, respectively ($n = 3$ mice per time point). **b**, Force-directed layout view of microglia subsets with partition-based graph abstraction vectors colored by cell subset. **d**, Distribution of expression of *Ccl2* by astrocyte (left) and microglia (right) subsets at 0.5 d.p.c. (astrocytes, $n = 586$ cells; Astro^{IFN}, $n = 32$; *lfg2*⁺ astrocytes, $n = 262$; reactive astrocytes, $n = 299$; microglia, $n = 1,970$; microglia^{IFN}, $n = 151$); exp., expression. **e**, Distribution of *lfit3* expression levels at each time point in MG (left: 0 d.p.c., $n = 12,757$; 0.5 d.p.c., $n = 7,064$; 1 d.p.c., $n = 7,626$; 2 d.p.c., $n = 8,417$; 4 d.p.c., $n = 5,741$; 7 d.p.c., $n = 6,635$; 14 d.p.c., $n = 6,235$) and astrocytes (right: values of n are the same as in Fig. 3k). In **d** and **e**, *** $P < 0.001$ (logistic regression likelihood ratio test; P values adjusted with the Benjamini-Hochberg method for multiple comparisons). Box plots

denote medians and IQRs; whiskers are the lowest datum still within 1.5 \times the IQR of the lower quartile and the highest datum still within 1.5 \times the IQR of the upper quartile. **f**, Representative IHC on retinal sections from 0 and 7 d.p.c. stained for IFIT3 (green) and GFAP⁺ astrocytes and MG (red; $n = 3$ mice per time point); blue, DAPI. **g**, Distribution of an Astro^{IFN} signature score across astrocytes from LPS-induced inflammation³³ classified to ONC astrocyte subsets (Student's t -test, one sided). **h**, Distribution of MCP1 expression scores across astrocytes, microglia and MG from uninjured (control, gray) and ONC (light blue) retinas. **i**, Average expression (z score, red/blue bar) of upregulated genes (columns) in MCP1 sorted by cell type and across time (right color bar). The blue and red ticks indicate IFN- and DAM-related genes (enrichment of IFN-response and DAM genes was determined by Fisher's exact test; $P < 0.001$). **j**, Dot plot showing expression of MCP1 DAM genes on microglia across time. **k**, Distribution of *lfnb1* and *lfn* expression by retinal cell types (x axis) across time. **l**, Representative IHC for IFIT3 (green) and GFAP (red) on retinal sections at 7 d.p.c. from PLX5622-treated mice (PLX) and untreated controls (ONC; $n = 3$ mice per condition); scale bars, 50 μ m.



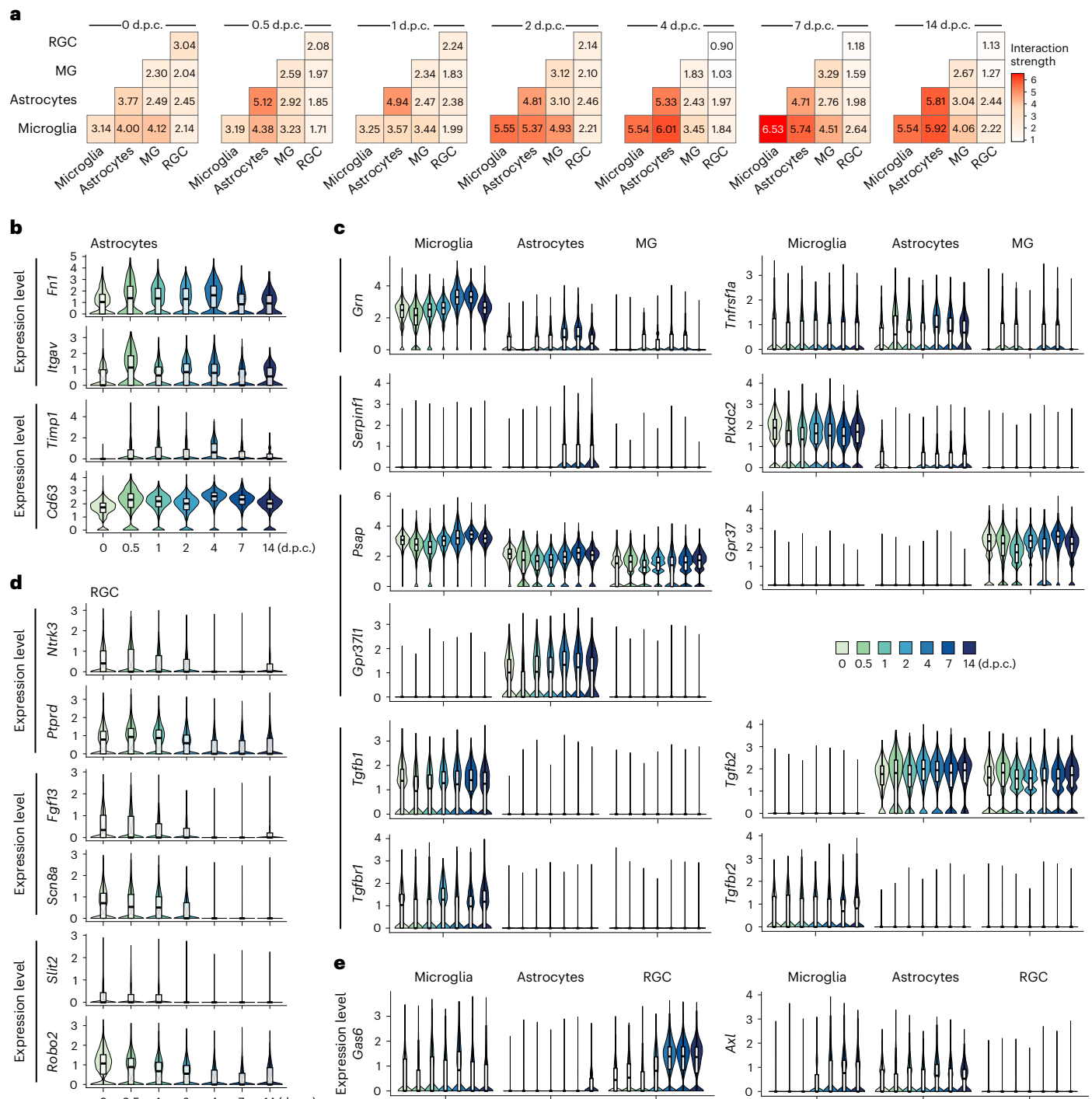


Fig. 7 | Multicellular interactions in the injured retina involve glial activity and decreased RGC function. a, Changes in interaction strength between pairs of retinal cell types (RGCs, MG, astrocytes and microglia) across time (0, 0.5, 1, 2, 4, 7 and 14 d.p.c.). **b–e**, Distribution of expression across time of genes encoding

RL pairs by RGCs ($n = 71,055$ cells), MG ($n = 54,565$), astrocytes ($n = 18,959$) and microglia ($n = 24,559$). Box plots denote medians and IQRs; whiskers are the lowest datum still within $1.5 \times$ the IQR of the lower quartile and the highest datum still within $1.5 \times$ the IQR of the upper quartile.

myeloid cells, showed diminished IFIT3 and higher GFAP expression by IHC, indicating increased glial reactivation (Fig. 6l). Thus, ONC involved co-regulation between glia and myeloid cells, with microglia the likely predominant source of IFN.

Multicellular interactions in the retina change after injury

To assess other cell–cell interactions regulating cellular dynamics and impacting RGCs after ONC, we computed potential RL interactions

between all the major retinal resident cells, including RGCs⁷. Across all time points, microglia were the strongest interactors (Fig. 7a), illustrating their constant microenvironmental surveillance. At 0.5–1 d.p.c., astrocytes were prominent interactors, including through extracellular matrix remodeling genes (for example, *Fn1–Itgav* and *Timp1–Cd63*; Fig. 7b) and the interleukin-1 axis (Supplementary Note 2). At 7–14 d.p.c., interactions involving microglia, astrocytes and MG reflected immunoregulation and restoration of homeostasis

(for example, *Grn-Tnfrsf1a*⁵⁸, *Serpinf1-Plxdc2* (ref. ⁵⁹), *Psap-Gpr37/Gpr37II* (ref. ⁶⁰) and the transforming growth factor- β axis⁶¹; Fig. 7c). RGC–RGC interactions weakened from 4 d.p.c. (for example, neurotrophic signaling (*Ntrk3-Ptprd*), neuronal firing (*Fgf13-Scn8a*) and axon guidance (*Slit2-Robo2*); Fig. 7a,d), reflecting a decline of injured RGC homeostatic functions⁷. Similarly, at 4 d.p.c., RGC–MG interactions weakened (Fig. 7a), including adhesion molecules that modulate neuronal functions (*Nlgn1-Nrxn2/Nrxn3* and *Slitrk2-Ptprs/Ptprd*). While RGC–astrocyte and RGC–microglia interaction strengths remained similar over time (Fig. 7a), RL pairs at the later time points included *Axl-Gas6* (Fig. 7e), which might mediate phagocytic clearance of apoptotic RGCs⁶². The limited change in RGC interactions may be due to their death, the dominance of RGC-intrinsic events or because the dearth of interactions contributes to RGC death. Finally, we used our atlas to assess the expression of genes in mice whose human orthologs are associated with human retinal diseases (Supplementary Note 4). Collectively, these findings highlighted the dynamic multicellular events associated with RGC degeneration (Extended Data Fig. 8).

Discussion

Here, we charted the tissue response to severe acute CNS injury and provided an atlas of the non-neuronal cells in the retina during this process.

While a coordinated IFN response was activated after injury, MG^{IFN}, Astro^{IFN} and microglia^{IFN} were present at baseline. Anti-inflammatory astrocytes are also present in the uninjured spinal cord⁶³, and rare IFN-response microglia are present in the healthy brain⁵³. It is possible that homeostatic IFN signaling may keep low-grade inflammation in check, with resident cells poised to rapidly respond to perturbation⁶³. Supporting this, early chemokine expression by astrocytes and microglia was higher in Astro^{IFN} and microglia^{IFN}. Further activation of the IFN program 4–7 d.p.c. coincided with peak RGC loss⁷, possibly in response to DNA damage during RGC apoptosis⁵². Future studies are needed to elucidate this response and to determine whether this is primarily a type I or type II response. Although there were a few *lfng*-expressing retinal T and NK cells, microglia, the most abundant retinal IFN producer, expressed *lfnb1*, and their depletion reduced the IFN signal, suggesting a predominantly type I response. Retinal type I IFN signaling is mostly associated with protective immunosuppression^{64,65}, suggesting that its expansion after injury may help with later inflammatory resolution. In a spinal cord injury model, PLX-mediated microglia depletion decreased ISG expression and impaired recovery⁶⁶. Moreover, an IFN program was activated in RGCs by regenerative interventions after ONC⁹. In microglia, type I IFN and DAM programs correlate and partly overlap in aging and neurodegeneration^{16,26,52,67}. These programs in ONC may be related to clearance of dying RGCs²⁹. The type I IFN response was activated during microglial renewal in the adult retina after injury and in the repopulation of brain microglia after depletion^{54,55}, but its involvement in homeostatic microglia self-renewal remains to be studied.

Spatially segregated MHC class II^{hi} and MHC class II^{lo} resident macrophages recur across mouse and human tissues^{45,68}. We identified non-microglial resident retinal *Ms4a7*^{hi} MHC class II^{hi} and *Ms4a7*^{lo} MHC class II^{lo} macrophages and characterized BAMs at the oBRB, whose molecular markers were previously lacking¹⁷. The localization of resident macrophages at border regions implicates them as tissue sentinels⁶⁹. Future studies can help define their functional relevance.

Our findings support a model where, during ONC, CCR2⁺ monocytes give rise to *Ms4a7*⁺ and *Gpnmb*⁺ macrophage subsets. Whether these cells integrate as resident macrophages is unknown. Most brain BAMs are derived from embryonic precursors, but in adulthood, meningeal and choroid plexus macrophages are replenished by circulating monocytes^{22,23}. At baseline, the vast majority of retinal resident macrophages are of embryonic origin, but a population of shorter-lived MHC class II^{hi} macrophages has been described^{16,30}. These distinctions

are blurred in ONC and other neuroinflammatory conditions, where blood-derived myeloid cells infiltrate, and resident macrophages change phenotypically²⁴. As resident macrophages are prone to replacement by blood-derived myeloid cells after injury⁶⁹, ONC might invoke similar replacement. Fate mapping and spatial genomics can help decipher this.

Gpnmb⁺ macrophages expressed genes associated with lipid metabolism and phagocytosis (for example, *Lgals3*, *Lpl*, *Cd63*, *Cd68* and *Spp1*), which were also enriched in microglia at 4–7 d.p.c., reminiscent of the DAM signature^{28,29}. Similar profiles were described in microglia and monocyte-derived macrophages in different CNS pathologies^{16,30,47,48} and in microglia in the early postnatal brain²⁶ and retina during developmental neuronal apoptosis⁷⁰. Outside the CNS, similar signatures were reported in tissue-resident and monocyte-derived macrophages from various healthy and pathological contexts^{45,46}. This program may function in non-myeloid cells, as we report in the injury-induced C12RPE subset. Selectively and temporally perturbing these populations could provide functional insight or translational value.

In conclusion, our atlas of non-neuronal cells in the adult mouse retina helped identify key events during neuronal degeneration. Many of these features recur in other CNS pathologies, offering a broadly applicable resource for neuroimmunology and CNS repair.

Online content

Any methods, additional references, Nature Portfolio reporting summaries, source data, extended data, supplementary information, acknowledgements, peer review information; details of author contributions and competing interests; and statements of data and code availability are available at <https://doi.org/10.1038/s41590-023-01437-w>.

References

- Gadani, S. P., Walsh, J. T., Lukens, J. R. & Kipnis, J. Dealing with danger in the CNS: the response of the immune system to injury. *Neuron* **87**, 47–62 (2015).
- Shechter, R. & Schwartz, M. CNS sterile injury: just another wound healing? *Trends Mol. Med.* **19**, 135–143 (2013).
- Burda, J. E. & Sofroniew, M. V. Reactive gliosis and the multicellular response to CNS damage and disease. *Neuron* **81**, 229–248 (2014).
- Andries, L., De Groef, L. & Moons, L. Neuroinflammation and optic nerve regeneration: where do we stand in elucidating underlying cellular and molecular players? *Curr. Eye Res.* **45**, 397–409 (2020).
- Greenhalgh, A. D., David, S. & Bennett, F. C. Immune cell regulation of glia during CNS injury and disease. *Nat. Rev. Neurosci.* **21**, 139–152 (2020).
- Williams, P. R., Benowitz, L. I., Goldberg, J. L. & He, Z. Axon regeneration in the mammalian optic nerve. *Annu. Rev. Vis. Sci.* **6**, 195–213 (2020).
- Tran, N. M. et al. Single-cell profiles of retinal ganglion cells differing in resilience to injury reveal neuroprotective genes. *Neuron* **104**, 1039–1055 (2019).
- Bray, E. R. et al. Thrombospondin-1 mediates axon regeneration in retinal ganglion cells. *Neuron* **103**, 642–657 (2019).
- Jacobi, A. et al. Overlapping transcriptional programs promote survival and axonal regeneration of injured retinal ganglion cells. *Neuron* **110**, 2625–2645 (2022).
- Moalem, G. et al. Autoimmune T cells protect neurons from secondary degeneration after central nervous system axotomy. *Nat. Med.* **5**, 49–55 (1999).
- Sas, A. R. et al. A new neutrophil subset promotes CNS neuron survival and axon regeneration. *Nat. Immunol.* **21**, 1496–1505 (2020).

12. Kurimoto, T. et al. Neutrophils express oncomodulin and promote optic nerve regeneration. *J. Neurosci.* **33**, 14816–14824 (2013).
13. Guttenplan, K. A. et al. Neurotoxic reactive astrocytes drive neuronal death after retinal injury. *Cell Rep.* **31**, 107776 (2020).
14. London, A. et al. Neuroprotection and progenitor cell renewal in the injured adult murine retina requires healing monocyte-derived macrophages. *J. Exp. Med.* **208**, 23–39 (2011).
15. Benhar, I., Reemst, K., Kalchenko, V. & Schwartz, M. The retinal pigment epithelium as a gateway for monocyte trafficking into the eye. *EMBO J.* **35**, 1219–1235 (2016).
16. O’Koren, E. G. et al. Microglial function is distinct in different anatomical locations during retinal homeostasis and degeneration. *Immunity* **50**, 723–737 (2019).
17. McMenamin, P. G., Saban, D. R. & Dando, S. J. Immune cells in the retina and choroid: two different tissue environments that require different defenses and surveillance. *Prog. Retin. Eye Res.* **70**, 85–98 (2019).
18. Geisert, E. E. et al. Gene expression in the mouse eye: an online resource for genetics using 103 strains of mice. *Mol. Vis.* **15**, 1730–1763 (2009).
19. Youkilis, J. C. & Bassnett, S. Single-cell RNA-sequencing analysis of the ciliary epithelium and contiguous tissues in the mouse eye. *Exp. Eye Res.* **213**, 108811 (2021).
20. Lehmann, G. L. et al. Single-cell profiling reveals an endothelium-mediated immunomodulatory pathway in the eye choroid. *J. Exp. Med.* **217**, e20190730 (2020).
21. Korin, B. et al. High-dimensional, single-cell characterization of the brain’s immune compartment. *Nat. Neurosci.* **20**, 1300–1309 (2017).
22. Mrdjen, D. et al. High-dimensional single-cell mapping of central nervous system immune cells reveals distinct myeloid subsets in health, aging, and disease. *Immunity* **48**, 380–395 (2018).
23. Van Hove, H. et al. A single-cell atlas of mouse brain macrophages reveals unique transcriptional identities shaped by ontogeny and tissue environment. *Nat. Neurosci.* **22**, 1021–1035 (2019).
24. Jordão, M. J. C. et al. Single-cell profiling identifies myeloid cell subsets with distinct fates during neuroinflammation. *Science* **363**, eaat7554 (2019).
25. Vecino, E., David Rodriguez, F., Ruzafa, N., Pereiro, X. & Sharma, S. C. Glia-neuron interactions in the mammalian retina. *Prog. Retin. Eye Res.* **51**, 1–40 (2016).
26. Hammond, T. R. et al. Single-cell RNA sequencing of microglia throughout the mouse lifespan and in the injured brain reveals complex cell-state changes. *Immunity* **50**, 253–271 (2019).
27. Ronning, K. E., Karlen, S. J., Miller, E. B. & Burns, M. E. Molecular profiling of resident and infiltrating mononuclear phagocytes during rapid adult retinal degeneration using single-cell RNA sequencing. *Sci. Rep.* **9**, 4858 (2019).
28. Krasemann, S. et al. The TREM2–APOE pathway drives the transcriptional phenotype of dysfunctional microglia in neurodegenerative diseases. *Immunity* **47**, 566–581 (2017).
29. Keren-Shaul, H. et al. A unique microglia type associated with restricting development of Alzheimer’s disease. *Cell* **169**, 1276–1290 (2017).
30. Wieghofer, P. et al. Mapping the origin and fate of myeloid cells in distinct compartments of the eye by single-cell profiling. *EMBO J.* **40**, e105123 (2021).
31. Hoang, T. et al. Gene regulatory networks controlling vertebrate retinal regeneration. *Science* **370**, eabb8598 (2020).
32. Habib, N. et al. Disease-associated astrocytes in Alzheimer’s disease and aging. *Nat. Neurosci.* **23**, 701–706 (2020).
33. Hasel, P., Rose, I. V. L., Sadick, J. S., Kim, R. D. & Liddelow, S. A. Neuroinflammatory astrocyte subtypes in the mouse brain. *Nat. Neurosci.* **24**, 1475–1487 (2021).
34. Zamanian, J. L. et al. Genomic analysis of reactive astrogliosis. *J. Neurosci.* **32**, 6391–6410 (2012).
35. Liddelow, S. A. et al. Neurotoxic reactive astrocytes are induced by activated microglia. *Nature* **541**, 481–487 (2017).
36. Qu, J. & Jakobs, T. C. The time course of gene expression during reactive gliosis in the optic nerve. *PLoS ONE* **8**, e67094 (2013).
37. Wohl, S. G., Schmeer, C. W., Kretz, A., Witte, O. W. & Isenmann, S. Optic nerve lesion increases cell proliferation and nestin expression in the adult mouse eye in vivo. *Exp. Neurol.* **219**, 175–186 (2009).
38. Babcock, A. A., Kuziel, W. A., Rivest, S. & Owens, T. Chemokine expression by glial cells directs leukocytes to sites of axonal injury in the CNS. *J. Neurosci.* **23**, 7922–7930 (2003).
39. Bosch, M. et al. Mammalian lipid droplets are innate immune hubs integrating cell metabolism and host defense. *Science* **370**, eaay8085 (2020).
40. Zahabi, A. et al. A new efficient protocol for directed differentiation of retinal pigmented epithelial cells from normal and retinal disease induced pluripotent stem cells. *Stem Cells Dev.* **21**, 2262–2272 (2012).
41. Zhao, C. et al. mTOR-mediated dedifferentiation of the retinal pigment epithelium initiates photoreceptor degeneration in mice. *J. Clin. Invest.* **121**, 369–383 (2011).
42. Yang, J.-Y. et al. Retinal protection by sustained nanoparticle delivery of oncostatin M and ciliary neurotrophic factor into rodent models of retinal degeneration. *Transl. Vis. Sci. Technol.* **10**, 6 (2021).
43. Reinhard, J., Roll, L. & Faissner, A. Tenascins in retinal and optic nerve neurodegeneration. *Front. Integr. Neurosci.* **11**, 30 (2017).
44. Shemer, A. et al. Engrafted parenchymal brain macrophages differ from microglia in transcriptome, chromatin landscape and response to challenge. *Nat. Commun.* **9**, 5206 (2018).
45. Eraslan, G. et al. Single-nucleus cross-tissue molecular reference maps toward understanding disease gene function. *Science* **376**, eabl4290 (2022).
46. Jaitin, D. A. et al. Lipid-associated macrophages control metabolic homeostasis in a Trem2-dependent manner. *Cell* **178**, 686–698 (2019).
47. Absinta, M. et al. A lymphocyte–microglia–astrocyte axis in chronic active multiple sclerosis. *Nature* **597**, 709–714 (2021).
48. Margeta, M. A. et al. Apolipoprotein E4 impairs the response of neurodegenerative retinal microglia and prevents neuronal loss in glaucoma. *Immunity* **55**, 1627–1644 (2022).
49. O’Koren, E. G., Mathew, R. & Saban, D. R. Fate mapping reveals that microglia and recruited monocyte-derived macrophages are definitively distinguishable by phenotype in the retina. *Sci. Rep.* **6**, 20636 (2016).
50. Xu, H., Dawson, R., Forrester, J. V. & Liversidge, J. Identification of novel dendritic cell populations in normal mouse retina. *Invest. Ophthalmol. Vis. Sci.* **48**, 1701–1710 (2007).
51. Yona, S. et al. Fate mapping reveals origins and dynamics of monocytes and tissue macrophages under homeostasis. *Immunity* **38**, 79–91 (2013).
52. Mathys, H. et al. Temporal tracking of microglia activation in neurodegeneration at single-cell resolution. *Cell Rep.* **21**, 366–380 (2017).
53. Sala Frigerio, C. et al. The major risk factors for Alzheimer’s disease: age, sex, and genes modulate the microglia response to A β plaques. *Cell Rep.* **27**, 1293–1306 (2019).
54. Zhan, L. et al. Proximal recolonization by self-renewing microglia re-establishes microglial homeostasis in the adult mouse brain. *PLoS Biol.* **17**, e3000134 (2019).
55. Huang, Y. et al. Repopulated microglia are solely derived from the proliferation of residual microglia after acute depletion. *Nat. Neurosci.* **21**, 530–540 (2018).

56. Rothhammer, V. et al. Type I interferons and microbial metabolites of tryptophan modulate astrocyte activity and central nervous system inflammation via the aryl hydrocarbon receptor. *Nat. Med.* **22**, 586–597 (2016).
57. Mostafavi, S. et al. Parsing the interferon transcriptional network and its disease associations. *Cell* **164**, 564–578 (2016).
58. Kuse, Y., Tsuruma, K., Mizoguchi, T., Shimazawa, M. & Hara, H. Progranulin deficiency causes the retinal ganglion cell loss during development. *Sci. Rep.* **7**, 1679 (2017).
59. Vigneswara, V., Berry, M., Logan, A. & Ahmed, Z. Pigment epithelium-derived factor is retinal ganglion cell neuroprotective and axogenic after optic nerve crush injury. *Invest. Ophthalmol. Vis. Sci.* **54**, 2624–2633 (2013).
60. Jolly, S. et al. G protein-coupled receptor 37-like 1 modulates astrocyte glutamate transporters and neuronal NMDA receptors and is neuroprotective in ischemia. *Glia* **66**, 47–61 (2018).
61. Ma, W. et al. Absence of TGF β signaling in retinal microglia induces retinal degeneration and exacerbates choroidal neovascularization. *eLife* **8**, e42049 (2019).
62. Fourgeaud, L. et al. TAM receptors regulate multiple features of microglial physiology. *Nature* **532**, 240–244 (2016).
63. Sanmarco, L. M. et al. Gut-licensed IFN γ ⁺ NK cells drive LAMP1⁺TRAIL⁺ anti-inflammatory astrocytes. *Nature* **590**, 473–479 (2021).
64. Lückoff, A. et al. Interferon- β signaling in retinal mononuclear phagocytes attenuates pathological neovascularization. *EMBO Mol. Med.* **8**, 670–678 (2016).
65. Wang, W. et al. Type I interferon therapy limits CNS autoimmunity by inhibiting CXCR3-mediated trafficking of pathogenic effector T cells. *Cell Rep.* **28**, 486–497 (2019).
66. Brennan, F. H. et al. Microglia coordinate cellular interactions during spinal cord repair in mice. *Nat. Commun.* **13**, 4096 (2022).
67. Roy, E. R. et al. Type I interferon response drives neuroinflammation and synapse loss in Alzheimer disease. *J. Clin. Invest.* **130**, 1912–1930 (2020).
68. Chakarov, S. et al. Two distinct interstitial macrophage populations coexist across tissues in specific subtissular niches. *Science* **363**, eaau0964 (2019).
69. Kierdorf, K., Masuda, T., Jordão, M. J. C. & Prinz, M. Macrophages at CNS interfaces: ontogeny and function in health and disease. *Nat. Rev. Neurosci.* **20**, 547–562 (2019).
70. Anderson, S. R. et al. Developmental apoptosis promotes a disease-related gene signature and independence from CSF1R signaling in retinal microglia. *Cell Rep.* **27**, 2002–2013 (2019).

Publisher's note Springer Nature remains neutral with regard to jurisdictional claims in published maps and institutional affiliations.

Springer Nature or its licensor (e.g. a society or other partner) holds exclusive rights to this article under a publishing agreement with the author(s) or other rightsholder(s); author self-archiving of the accepted manuscript version of this article is solely governed by the terms of such publishing agreement and applicable law.

© Springer Nature America, Inc. 2023

Methods

Mice

All animal experiments were approved by the Institutional Animal Care and Use Committees at Harvard University and Children's Hospital, Boston. Mice were maintained in pathogen-free facilities under standard housing conditions with continuous access to food and water. All experiments were performed in adult mice from 6 to 16 weeks of age and included both males and females. The following mouse strains were used: C57BL/6J (JAX, 000664), *Vglut2*-IRES-*cre* (*Slc17a6*^{tm2(cre)Low1/J71}) crossed to the Cre-dependent reporter Thy1-STOP-YFP line 15 (B6.Cg-Tg(Thy1-EYFP)15Jrs/J⁷²) and *Ccr2*^{RF} (B6.129(Cg)-*Ccr2*^{tm2.Ilf/J}; JAX, 017586)⁷³ crossed to C57BL/6J mice to generate heterozygotes.

ONC

ONC injury was performed as previously described⁷¹⁵. Briefly, after anesthesia with ketamine/xylazine (ketamine 100–120 mg kg⁻¹ and xylazine 10 mg kg⁻¹), the optic nerve was exposed intraorbitally and crushed with fine forceps (Dumont 5, FST) for 2 s approximately 0.5–1 mm behind the optic disc. All surgeries were performed by an experienced surgeon who visually confirmed ONC during the procedure.

Cell preparation and flow cytometry

Mice were intracardially perfused with PBS. After dissection, eyes were visually inspected for damage or blood, which were used as criteria for exclusion.

Retina. Eyes were dissected in AMES solution (equilibrated with 95% O₂ and 5% CO₂). Retinas, separated from the eyecup and ciliary body, were digested in papain and dissociated to single-cell suspensions using manual trituration in ovomucoid solution. Cells were centrifuged at 450g for 8 min and resuspended in AMES + 4% bovine serum albumin (BSA) to a concentration of 10 million cells per 100 ml.

RPE. RPE sheets were isolated from posterior eyecups based on a protocol adapted from Fernandez-Godino et al.⁷⁴. Briefly, eyecups were dissected in HBSS⁺+HEPES and incubated in 0.25% trypsin/EDTA for 45 min at 37 °C, after which RPE sheets were released by manual shaking into 20% fetal bovine serum in HBSS⁺+HEPES, centrifuged at 340g for 2 min and incubated in 0.05% trypsin/EDTA for 10 min at 37 °C. Cells were washed, resuspended and triturated 50 times in 5% fetal bovine serum/HBSS⁺+HEPES and filtered for staining and cell sorting. For scRNA-seq experiments, eyecups from four to eight mice were pooled per condition.

The following antibodies were used and conjugated to various fluorophores: anti-CD90.2 (Thy1.2, clone 53-2.1, Thermo Fisher Scientific), CD45 (clone 30-F11, BD Pharmingen), CD11b (clone MI/70, BioLegend), CD115 (clone AFS98, BioLegend), Ly6C (clone HK1.4, BioLegend), CD140a (clone APA5, BioLegend) and GLAST (clone ACSA-1, Miltenyi Biotec). A detailed list is included in Supplementary Table 4. Cells were incubated with antibodies for 15 min, washed with an excess of medium, centrifuged and resuspended again in AMES + 4% BSA at a concentration of 7 million cells per ml. The live cell marker Calcein Blue (Thermo Fisher Scientific) was added just before FACS. Cellular debris, doublets and dead cells were excluded, and cells were sorted on a MoFlo Astrios (Beckman Coulter) through a 100- μ m nozzle using the 'Purity' mask. For scRNA-seq, cells were gated on CD45, GLAST (EAAT1, *Slc1a3*) and CD140a (PDGFR α) to enrich for immune cells, MG and astrocytes, respectively. Because GLAST is expressed by both MG and astrocytes, and the former are much more abundant, astrocytes were specifically enriched using the marker CD140a (PDGFR α), which is expressed by retinal astrocytes^{75,76}. Cells were collected into 100 μ l of AMES + 4% BSA per 25,000 sorted cells. Following collection, cells were centrifuged and resuspended in PBS + 0.1% non-acetylated BSA at a concentration range of 500–2,000 cells per μ l for droplet-based scRNA-seq per the

manufacturer's instructions (10x Genomics). From the retina, two to five independent experiments were performed for scRNA-seq per time point. In each experiment, retinas from two to eight mice were pooled to collect enough cells for sequencing. Because MG are the most abundant of our enriched cell populations, they were separately loaded into independent channels, whereas the rarer cell types were pooled together and loaded together into channels. Thus, throughout the study, we only compared intracompartments frequencies of cell subsets across time points (for example, frequencies of different subsets of glia or of different subsets of immune cells) but not cross-compartment frequencies (for example, between immune and glia cells).

3'-Droplet-based scRNA-seq

Single-cell libraries were prepared using the a single-cell gene expression 3' v2 or v3 kit on the Chromium platform (10x Genomics) following the manufacturer's protocol. On average, approximately 7,000–12,000 single cells were loaded on each channel, and approximately 3,000–7,000 cells were recovered. Quantification and quality control analyses were performed using the Agilent Bioanalyzer high-sensitivity DNA assay. Libraries were sequenced on an Illumina NextSeq 500 or HiSeq X platforms (paired-end reads: read 1, 26 bases; read 2, 55 bases for NextSeq and 98 bases for HiSeq). From the retina, two to five independent experiments per time point were performed for scRNA-seq. From the eyecup, one experiment was performed for each time point.

Histological methods and imaging

Eyes were collected from mice intracardially perfused with 4% paraformaldehyde and postfixed in 4% paraformaldehyde for an additional 15–30 min or 1 h for RPE whole mounts. Eyes were transferred into PBS until dissection, following which retinas or eyecups were either used for whole-mount IHC or posterior eyecups were submerged in 30% sucrose and embedded in tissue freezing medium (OCT) to cryosection into 20- to 25- μ m-thick cross-sections. For formalin-fixed paraffin-embedded (FFPE) sections, eyes from mice intracardially perfused with PBS were postfixed in 10% formaldehyde at room temperature overnight and transferred to 70% ethanol before paraffin embedding and sectioning into 5- μ m-thick sections.

To immunostain retinal/RPE whole mounts, retinas or posterior eyecups with the retina removed were incubated in protein block (5% normal serum, 0.3% Triton X-100 and 1 \times PBS) for 3 h at room temperature or overnight at 4 °C, followed by incubation with primary antibodies (in protein block) for 3–7 d and secondary antibodies (in 1 \times PBS) overnight. All antibody incubations were performed at 4 °C with gentle rocking.

For IHC on cryosections, slides were incubated for 1 h in protein block, incubated with primary antibodies overnight and incubated with secondary antibodies for 2–3 h. Initial block and secondary antibody incubations were performed at room temperature, and primary antibody incubations were performed at 4 °C.

For IHC on FFPE sections, slides were baked at 60 °C for 30 min, followed by deparaffinization and rehydration through a series of successive incubations in xylenes, ethanol (100%, 95%, 70% and 50%) and finally distilled water. Antigen retrieval was performed with antigen unmasking solution (Vector Laboratories) in a vegetable steamer. Sections were blocked in CAS-Block histochemical reagent (Thermo Fisher Scientific) for 30 min at room temperature and incubated overnight with primary antibodies in CAS-Block at 4 °C in a humidified chamber. After washes in PBS, sections were incubated with secondary antibodies in PBS for 1 h at room temperature before mounting with DAPI. A detailed list of antibodies used in this study is included in Supplementary Table 4.

FISH was performed on FFPE sections using the commercially available RNAscope fluorescent multiplex assay (ACD) or on whole-mount retinas with HCR (Molecular Instruments), according to manufacturers' instructions.

Zeiss LSM 710 and Olympus FV-1000 confocal microscopes were used for imaging. Images were merged, cropped and optimized using ImageJ (Fiji)⁷⁷ and Adobe Photoshop and arranged using Adobe Illustrator.

Antibody treatment for monocyte depletion

CCR2⁺ monocytes were depleted by intraperitoneal injections of monoclonal antibody to CCR2 (MC-21 (ref. ⁷⁸); 400 µg) starting 1 d before ONC and every other day until the experimental endpoint (up to five injections). Depletion efficiency was confirmed in the blood using flow cytometry.

PLX5622 treatment for myeloid cell depletion

Mice were fed with control chow (AIN-76) or with chow containing 1,200 ppm of the CSF1R antagonist PLX5622 (Plexxikon), as previously described⁷⁹, starting 1 week before ONC and for an additional 1 week until the experimental endpoint.

scRNA-seq preprocessing

Cell Ranger 2.1.0 (10x Genomics) was used for read demultiplexing, alignment to the mouse genome and unique molecular identifier (UMI) counting and collapsing. The top 6,000 cells from each experiment with the largest number of UMIs were used for further analysis⁷. In total, 121,309 cells expressing at least 400 genes per cell were retained for downstream analysis.

Batch correction and clustering: retina

scSphere⁸⁰, a deep learning-based method, was used to merge all 121,309 cells from different time points by taking time after crush and mouse strain as the batch vectors. For scSphere analysis, a latent space of dimension 10 was used so each cell was mapped to a 10-sphere. The latent representation of cells was clustered using the Louvain community detection algorithm^{81,82} to produce 45 clusters. These clusters were assigned to 25 putative cell types/groups (including cell doublets and low-quality cell clusters) using a previously described automatic cell type assignment approach⁸³ followed by manual inspection (Fig. 1a,b). Cell clusters that expressed neuronal markers ('neurons'), expressed marker genes of two cell types ('contaminants') or had very small numbers of detected genes per cell and did not express cell subtype-specific marker genes ('low UMI') were discarded, retaining 107,067 cells assigned to 14 broad groups for further analysis. These 107,067 cells were partitioned into three categories by cell class: astrocytes (18,959 cells), MG (54,565 cells) and all other cells (33,543 cells, predominantly immune cells). As each cell category was separately enriched and sorted, we only calculated proportions between subsets within a category but not across the categories. To identify cell subtypes and very rare cell types, the cells from each compartment were then analyzed separately, either by reclustering these cells using the Louvain community detection algorithm^{81,82} implemented in Seurat⁸⁴, specifically using scSphere low-dimensional representations (astrocytes and MG), or by rerunning scSphere for batch correction and dimensionality reduction and reclustering scSphere results (immune cells). This analysis further identified three MG subsets (Fig. 3d), five astrocyte subsets (Fig. 3g) and 22 immune cell subsets, and removed another 3,116 'contaminant' cell profiles from the immune cell compartment, retaining 30,427 immune cells in total (including some stromal cell subsets) after filtering (Fig. 2a).

Batch correction and clustering: eyecup

The data were analyzed using the R package Seurat following previously described methods⁹. Briefly, cells collected at each time point were identified as one batch, and the function 'sctransform' was applied to each batch for normalization. The top 3,000 features were used for integration of all batches using the function 'IntegrateData'. Markers for each cluster were identified using the function 'FindAllMarkers'

with the 'Mast' algorithm. Cell types were annotated based on canonical markers. A low-quality RPE cluster was filtered post hoc based on high expression of mitochondrial genes together with a low number of genes per cell relative to the other RPE clusters.

Differential gene expression analysis

Logistic regression was used for differential gene expression analysis, taking both the log₂-transformed total number of detected genes in each cell and the mouse strain as covariates and the Seurat implementation for differential expression analysis⁸⁴.

Gene Ontology enrichment analysis

To identify biological processes enriched in RPE clusters, we tested for enrichment in Gene Ontology biological process gene sets from the Molecular Signatures Database^{85,86}, which uses the hypergeometric distribution.

Gene signature analysis

Gene signature scores were calculated, as previously described⁸⁷, with implementation in the Seurat package⁸⁴. The IFN gene signature was obtained from ImmGen⁵⁷.

MC-21 (monocyte depletion) data analysis

To help annotate cells from MC-21 antibody-treated mice and control mice, cell profiles were coembedded using scSphere⁸⁰ with all immune cell profiles (Fig. 2a). A *k*-nearest neighbor classifier (*k* = 15) trained on the immune cells with cell state annotations (Fig. 2a) was used to annotate cells from both control and MC-21-treated mice. Before this analysis, likely non-immune cell contaminants were first separately removed from the profiled cells from both control and MC-21-treated mice. Specifically, to remove these non-immune cells, the full analysis was performed with scSphere for batch correction and dimensionality reduction taking experiment as batch vector, and then scSphere's low-dimensional representations of cell profiles (in five dimensions) were clustered using the Louvain algorithm^{81,82} as implemented in Seurat⁸⁴. Non-immune cells were manually annotated and removed before further analysis.

Optimal transport and RNA velocity analysis

The Waddington-OT package⁸⁸ was used with default parameters as in the Waddington-OT online tutorial (<https://broadinstitute.github.io/wot/tutorial/>) to trace the likely ancestors of cells from two subsets of *Ms4a7⁺* macrophages.

For myeloid cell differentiation trajectory analysis, velocity⁸⁹ and scVelo⁹⁰ were used. Specifically, after running Cell Ranger, velocity was used to calculate the intronic and exonic UMIs for each cell passing the initial filtering, and then scVelo was used to calculate the likely differentiation potential for each cell. Although scVelo can be impacted by batch effects (for example, samples confounded with time), there was no apparent strong batch effect between monocytes, macrophages and DCs. Thus, scVelo was run with velocity results as inputs.

Identification of multicellular programs

The DIALOGUE method was used to identify multicellular programs⁹¹ only with resident cells (astrocytes, MG and microglia) without partitioning them into more granular cell states. We followed the default settings for DIALOGUE analysis. The number of MCP *k* was set to 6. We only considered 'ctrl' or 'crush' and tested the association of this binary feature with MCPs (DIALOGUE only supports binary feature for the current version, the 'pheno' parameter). DIALOGUE also takes batch vectors as covariant in analysis, and we used mouse strain as the 'conf' parameter. DIALOGUE needs the full non-sparse matrix of each compartment as an input. Thus, for each compartment, we randomly subsampled 20,000 cells for analysis if the total number of cells from that compartment was greater than 20,000.

RL-based interaction analysis

A set of 2,392 manually curated RL pairs (Supplementary Table 3), obtained from recent publications^{92,93} and manually updated (removing pairs that did not have mouse homologs or convincing literature support in mice, correcting homologs, ultimately adding 13 pairs), was used to identify putative cell–cell interactions between cell types.

There are several challenges for current methods for inferring the cell–cell interactions from scRNA-seq data. First, cell types expressing receptors or ligands whose cognate partner is highly expressed ubiquitously across all cells can become interaction hubs. Second, some methods consider only pairwise interactions but not multisubunit complexes. Third, because of measurement errors (for example, ambient RNAs), ligand or receptor expression can be detected at least at low levels in cell types that do not actually express these genes and will add noise to the interaction strength ranks between cell types. This is likely given the large number of RL pairs scored (above 2,000).

To address these problems, a k -nearest neighbor approach was used to estimate the interaction strength between cell types. Specifically, for a gene g of a cell type, its score s_g is defined as the total number of detected UMIs of gene g in that cell type divided by the total number of UMIs of gene g across all cell types. If g is a member of a multisubunit complex with m subunits, the weight for that complex is defined as the geometric mean of scores of all members. Then, the final interaction score between an RL pair is the product of the weights of the two interaction complexes. For any two cell types i and j , the interaction score is calculated for each RL pair. Finally, the interaction strength between two cell types is the sum of the top k interaction scores. These interaction strength scores are used to rank the interaction partners of a cell type. Only the top k interaction pairs were used to decrease the influence of the background interaction noise.

Astrocyte classifier analysis

To check for overlapping expression profiles of ONC astrocytes in astrocytes from other pathological conditions, data from LPS-induced inflammation³³ and experimental autoimmune encephalomyelitis⁹⁴ were analyzed. Because of batch effects between and within studies (for example, due to different scRNA-seq technologies, mouse strains and experimental time points), a neighborhood component analysis⁹⁵ was used to map our astrocytes to a 50-dimensional latent space, and the learned neighborhood component analysis mapping function was used to project the other datasets to the same 50-dimensional latent space. Next, a k -nearest neighbor classifier ($k = 11$) trained on our data was used to predict cell identities of the test data (all in the 50-dimensional latent space). To help visualize rare cell states (for example, Astro^{IFN}) such that they would not be obscured by abundant cell states, for astrocyte subsets with over 2,000 cells, we randomly subsampled 2,000 cells for presentation and created a uniform manifold approximation and projection (UMAP) using the subsampled data.

For validation, gene signatures of our Astro^{IFN} and reactive astrocyte subsets were scored on the predicted cells. Gene signatures for each subset were the top 100 upregulated genes in that subset compared to the main astrocyte subset. To establish the connection between our identified astrocyte subsets and the astrocytes identified by Hasel et al.³³, we additionally scored our astrocytes using their gene signatures. To further rule out the possibility that these astrocyte subsets were artifacts induced during cell dissociation, we also scored all astrocytes for a tissue dissociation signature⁹⁶.

Mapping disease genes

The retinal disease gene lists were generated from POAG⁹⁷ and VDD and VCDR⁹⁸ and all other diseases from the Retinal Information Network (RetNet, <https://sph.uth.edu/retnet/>), downloaded on 16 December 2021. Analysis was performed as previously described⁹⁹. Briefly, the retina and eyecup datasets were merged and renormalized before

plotting. Genes from each disease catalog were filtered to retain only those expressed in more than 10% of cells. Values were z scaled in each row of the heat map, and genes were ordered by the peak values in the columns.

Statistical analysis

Age- and genotype-matched mice were randomized for in vivo experiments with several groups. No statistical methods were used to pre-determine sample sizes, but our sample sizes are similar to those reported in previous publications⁷⁹ and were based on pilot experiments. Data distribution was assumed to be normal, but this was not formally tested. Retinas were excluded from analysis if ONC was incomplete or if signs of damage or bleeding were evident after dissection.

Reporting summary

Further information on research design is available in the Nature Portfolio Reporting Summary linked to this article.

Data availability

Data generated during this study have been deposited in Gene Expression Omnibus under accession number [GSE199317](https://www.ncbi.nlm.nih.gov/geo/query/acc.cgi?acc=GSE199317). The data can be visualized in the Broad Institute Single Cell Portal (https://singlecell.broadinstitute.org/single_cell/study/SCP1785).

Code availability

Scripts have been deposited to <https://bitbucket.org/jerry00/onc-retina-script/src/master/>.

References

- Vong, L. et al. Leptin action on GABAergic neurons prevents obesity and reduces inhibitory tone to POMC neurons. *Neuron* **71**, 142–154 (2011).
- Buffelli, M. et al. Genetic evidence that relative synaptic efficacy biases the outcome of synaptic competition. *Nature* **424**, 430–434 (2003).
- Saederup, N. et al. Selective chemokine receptor usage by central nervous system myeloid cells in CCR2–red fluorescent protein knock-in mice. *PLoS ONE* **5**, e13693 (2010).
- Fernandez-Godino, R., Garland, D. L. & Pierce, E. A. Isolation, culture and characterization of primary mouse RPE cells. *Nat. Protoc.* **11**, 1206–1218 (2016).
- Takahama, S. et al. Retinal astrocytes and GABAergic wide-field amacrine cells express PDGFR α : connection to retinal ganglion cell neuroprotection by PDGF-AA. *Invest. Ophthalmol. Vis. Sci.* **58**, 4703–4711 (2017).
- Macosko, E. Z. et al. Highly parallel genome-wide expression profiling of individual cells using nanoliter droplets. *Cell* **161**, 1202–1214 (2015).
- Schindelin, J. et al. Fiji: an open-source platform for biological-image analysis. *Nat. Methods* **9**, 676–682 (2012).
- Mack, M. et al. Expression and characterization of the chemokine receptors CCR2 and CCR5 in mice. *J. Immunol.* **166**, 4697–4704 (2001).
- Okunuki, Y. et al. Retinal microglia initiate neuroinflammation in ocular autoimmunity. *Proc. Natl Acad. Sci. USA* **116**, 9989–9998 (2019).
- Ding, J. & Regev, A. Deep generative model embedding of single-cell RNA-Seq profiles on hyperspheres and hyperbolic spaces. *Nat. Commun.* **12**, 2554 (2021).
- Blondel, V. D., Guillaume, J.-L., Lambiotte, R. & Lefebvre, E. Fast unfolding of communities in large networks. *J. Stat. Mech.* **2008**, P10008 (2008).
- Levine, J. H. et al. Data-driven phenotypic dissection of AML reveals progenitor-like cells that correlate with prognosis. *Cell* **162**, 184–197 (2015).

83. Ding, J. et al. Systematic comparison of single-cell and single-nucleus RNA-sequencing methods. *Nat. Biotechnol.* **38**, 737–746 (2020).
84. Hao, Y. et al. Integrated analysis of multimodal single-cell data. *Cell* **184**, 3573–3587 (2021).
85. Subramanian, A. et al. Gene set enrichment analysis: a knowledge-based approach for interpreting genome-wide expression profiles. *Proc. Natl Acad. Sci. USA* **102**, 15545–15550 (2005).
86. Liberzon, A. et al. The Molecular Signatures Database (MSigDB) hallmark gene set collection. *Cell Syst.* **1**, 417–425 (2015).
87. Tirosh, I. et al. Dissecting the multicellular ecosystem of metastatic melanoma by single-cell RNA-seq. *Science* **352**, 189–196 (2016).
88. Schiebinger, G. et al. Optimal-transport analysis of single-cell gene expression identifies developmental trajectories in reprogramming. *Cell* **176**, 928–943 (2019).
89. La Manno, G. et al. RNA velocity of single cells. *Nature* **560**, 494–498 (2018).
90. Bergen, V., Lange, M., Peidli, S., Wolf, F. A. & Theis, F. J. Generalizing RNA velocity to transient cell states through dynamical modeling. *Nat. Biotechnol.* **38**, 1408–1414 (2020).
91. Jerby-Arnon, L. & Regev, A. DIALOGUE maps multicellular programs in tissue from single-cell or spatial transcriptomics data. *Nat. Biotechnol.* **40**, 1467–1477 (2022).
92. Baccin, C. et al. Combined single-cell and spatial transcriptomics reveal the molecular, cellular and spatial bone marrow niche organization. *Nat. Cell Biol.* **22**, 38–48 (2020).
93. Hou, R., Denisenko, E., Ong, H. T., Ramilowski, J. A. & Forrest, A. R. Predicting cell-to-cell communication networks using NATMI. *Nat. Commun.* **11**, 5011 (2020).
94. Wheeler, M. A. et al. MAFG-driven astrocytes promote CNS inflammation. *Nature* **578**, 593–599 (2020).
95. Goldberger, J., Hinton, G. E., Roweis, S. & Salakhutdinov, R. R. Neighbourhood components analysis. In *Advances in Neural Information Processing Systems 17 (NIPS 2004)* (eds Saul, L. et al.) (MIT Press, 2004).
96. van den Brink, S. C. et al. Single-cell sequencing reveals dissociation-induced gene expression in tissue subpopulations. *Nat. Methods* **14**, 935–936 (2017).
97. Charakhani, P. et al. Genome-wide meta-analysis identifies 127 open-angle glaucoma loci with consistent effect across ancestries. *Nat. Commun.* **12**, 1258 (2021).
98. Han, X. et al. Automated AI labeling of optic nerve head enables insights into cross-ancestry glaucoma risk and genetic discovery in >280,000 images from UKB and CLSA. *Am. J. Hum. Genet.* **108**, 1204–1216 (2021).
99. van Zyl, T. et al. Cell atlas of the human ocular anterior segment: tissue-specific and shared cell types. *Proc. Natl Acad. Sci. USA* **119**, e2200914119 (2022).
- I. Shachar and M. Schwartz for helpful discussions, M. Schwartz and M. Mack for kindly providing the MC-21 antibody, Y. Okunuki and K. Connor for their help with the PLX experiment, L. Jerby-Arnon for assistance with the DIALOGUE analysis, K. Dey and K. Jagadeesh for help with genome-wide association study analysis, R. Harpaz for help with RPE image analysis and Z. Niziolek, S. Turney, Y. Li, R. Schaffer, M. Laboulaye, E. Martersteck, T. Delorey, D. Phillips and staff members of the Harvard University Bauer Core Facility and the Koch Institute Histology Core for technical assistance. We thank L. Gaffney and A. Hupalowska for help with figure preparation and the Richter family for support. This study was supported by the Human Frontier Science Program (I.B.), the Center for Integration in Science of the Israeli Ministry of Absorption (I.B.), HHMI (A.R.), the Klarman Family Foundation (A.R.), Wings for Life Spinal Cord Research Foundation (A.J.) and NIH grants EY028633 and MH105960 (J.R.S.). The funders had no role in the study design, experiments performed, data collection, data analysis and interpretation or preparation of the manuscript.

Author contributions

I.B. and A.R. conceived the study. I.B., I.E.W., K.S., J.R.S. and A.R. designed experiments and analyzed data. I.B., I.E.W., A.J., M.S., G.B., N.M.T. and C.W. performed experiments. J.D., W.Y. and K.S. developed computational approaches and analyzed scRNA-seq data. Z.H., J.R.S. and A.R. provided supervision and acquired funding. I.B., J.D. and A.R. wrote the manuscript, with input from all authors.

Competing interests

A.R. is a founder and equity holder of Celsius Therapeutics, an equity holder in Immunitas Therapeutics and, until 31 August 2020, was a SAB member of Syros Pharmaceuticals, Neogene Therapeutics, Asimov and Thermo Fisher Scientific. From 1 August 2020, A.R. is an employee of Genentech and has equity in Roche. J.R.S. is a consultant for Biogen. Z.H. is an advisor of Myro Therapeutics, Axonis and Rugen Therapeutics. The remaining authors declare no competing interests.

Additional information

Extended data is available for this paper at <https://doi.org/10.1038/s41590-023-01437-w>.

Supplementary information The online version contains supplementary material available at <https://doi.org/10.1038/s41590-023-01437-w>.

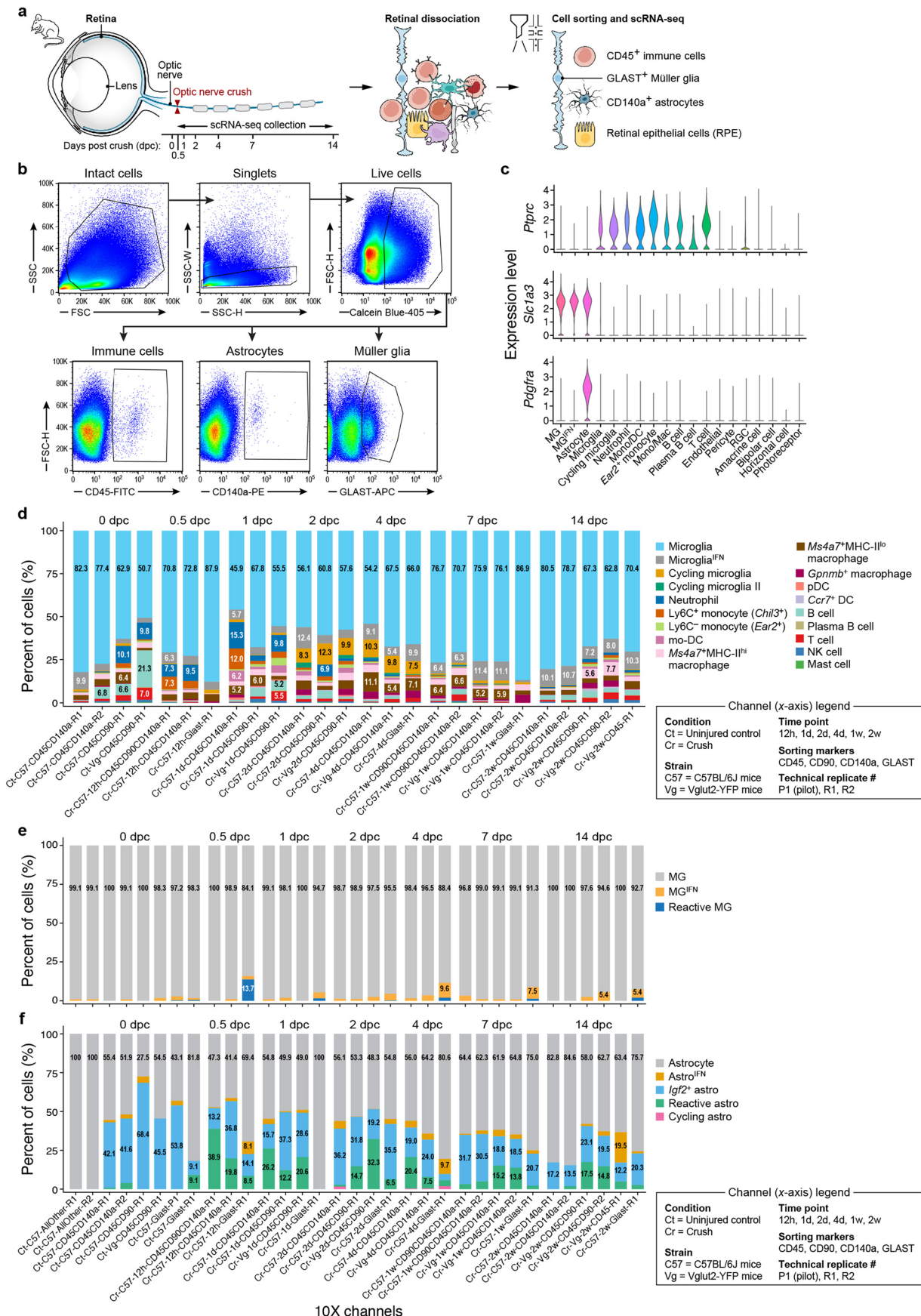
Correspondence and requests for materials should be addressed to Inbal Benhar or Aviv Regev.

Peer review information *Nature Immunology* thanks Daniel Saban and the other, anonymous, reviewer(s) for their contribution to the peer review of this work. Primary Handling Editor: Ioana Visan, in collaboration with the *Nature Immunology* team.

Reprints and permissions information is available at www.nature.com/reprints.

Acknowledgements

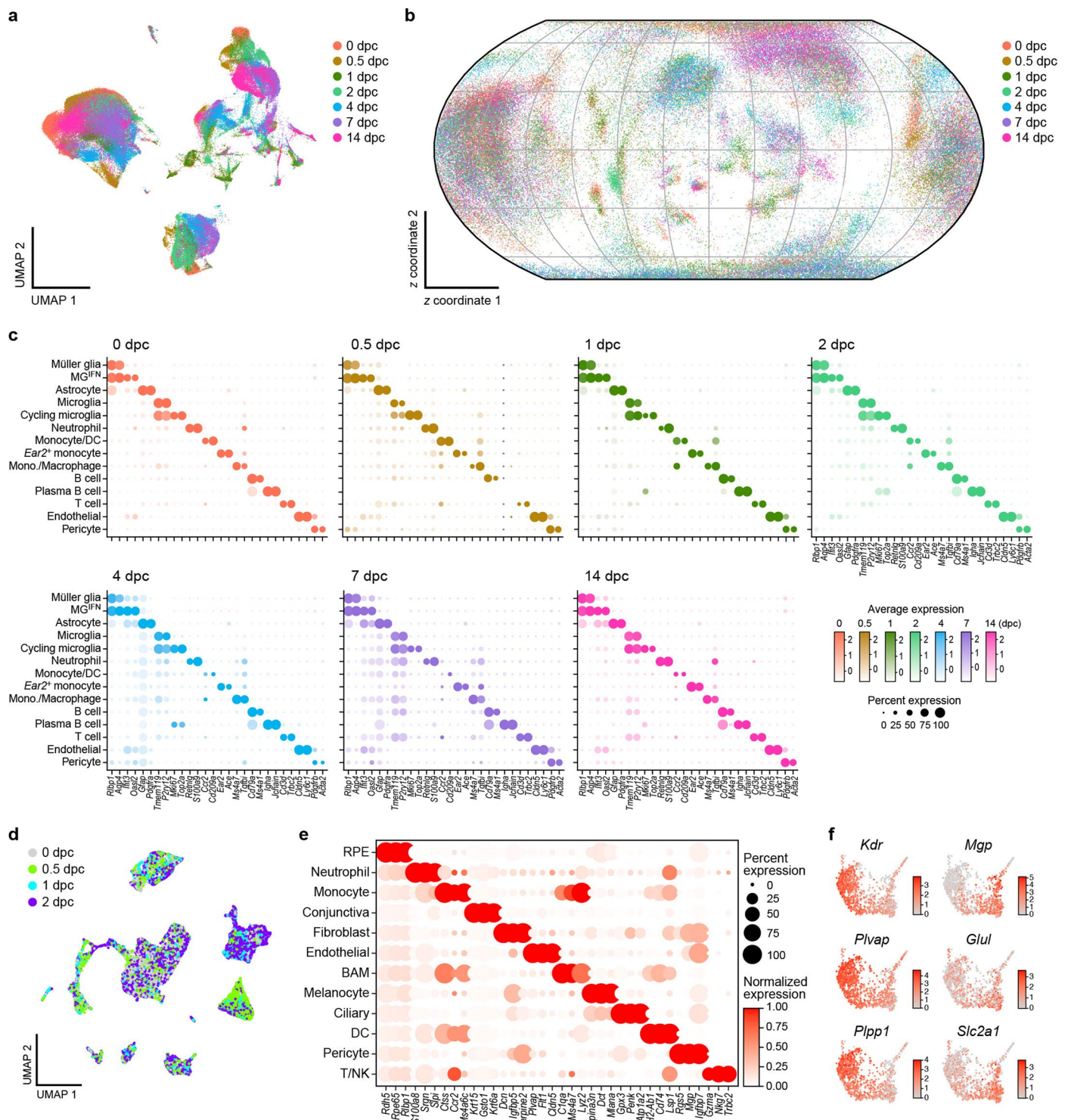
We acknowledge the authors whose work could not be cited due to space limitations. We thank I. Avraham-Davidi, T. van Zyl, R. Kedmi,



Extended Data Fig. 1 | Experimental strategy and reproducibility.

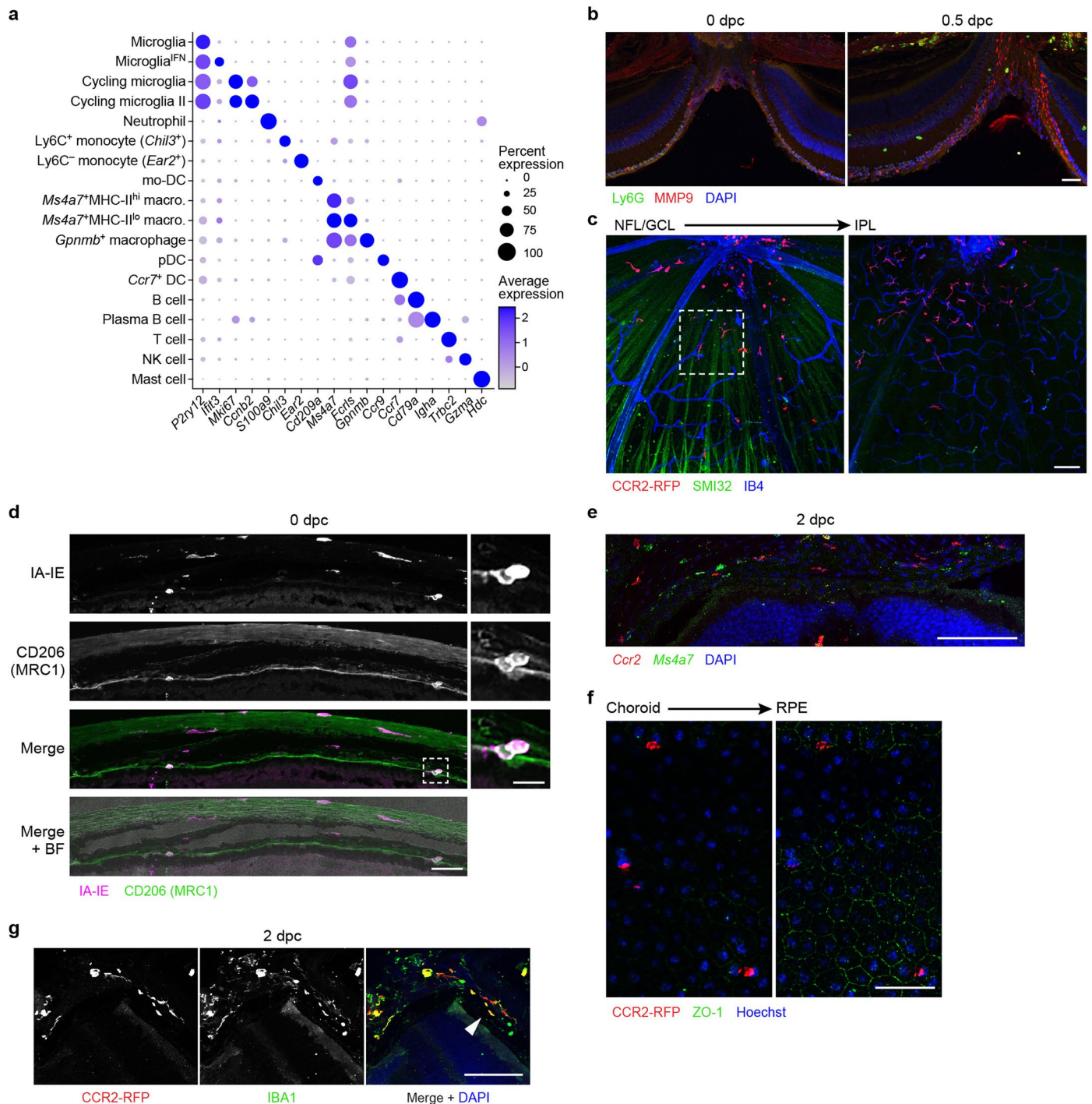
a, Experimental overview. **b**, Flow cytometry gating strategy used to enrich for retinal CD45⁺ immune cells, CD140a⁺ (Pdgfra⁺) astrocytes and GLAST⁺ Müller glia (MG). **c**, Distribution of expression levels of RNAs for the markers used

to sort immune (*Ptprc* = CD45), Müller glia (*Slc1a3* = GLAST), and astrocyte (*Pdgfra* = CD140a) subsets. **d-f**, Variation of cell composition across experiments. Fraction (y axis) of immune (**d**), MG (**e**) and astrocyte (**f**) subsets across 10X channels (x axis; legend).



Extended Data Fig. 2 | Changes in cell composition and stability in cell marker expression throughout the time course. **a**, 2D Uniform Manifold Approximation and Projection (UMAP) for 121,309 single cells profiled from the retina across 0, 0.5, 1, 2, 4, 7 and 14 dpc, colored by time point (legend). **b**, Sphere embedding of 121,309 single cell profiles from the retina, projected to 2D by the Equal Earth map projection method, colored by time point (legend). **c**, Fraction of expressing cells (dot size) and mean expression levels in expressing

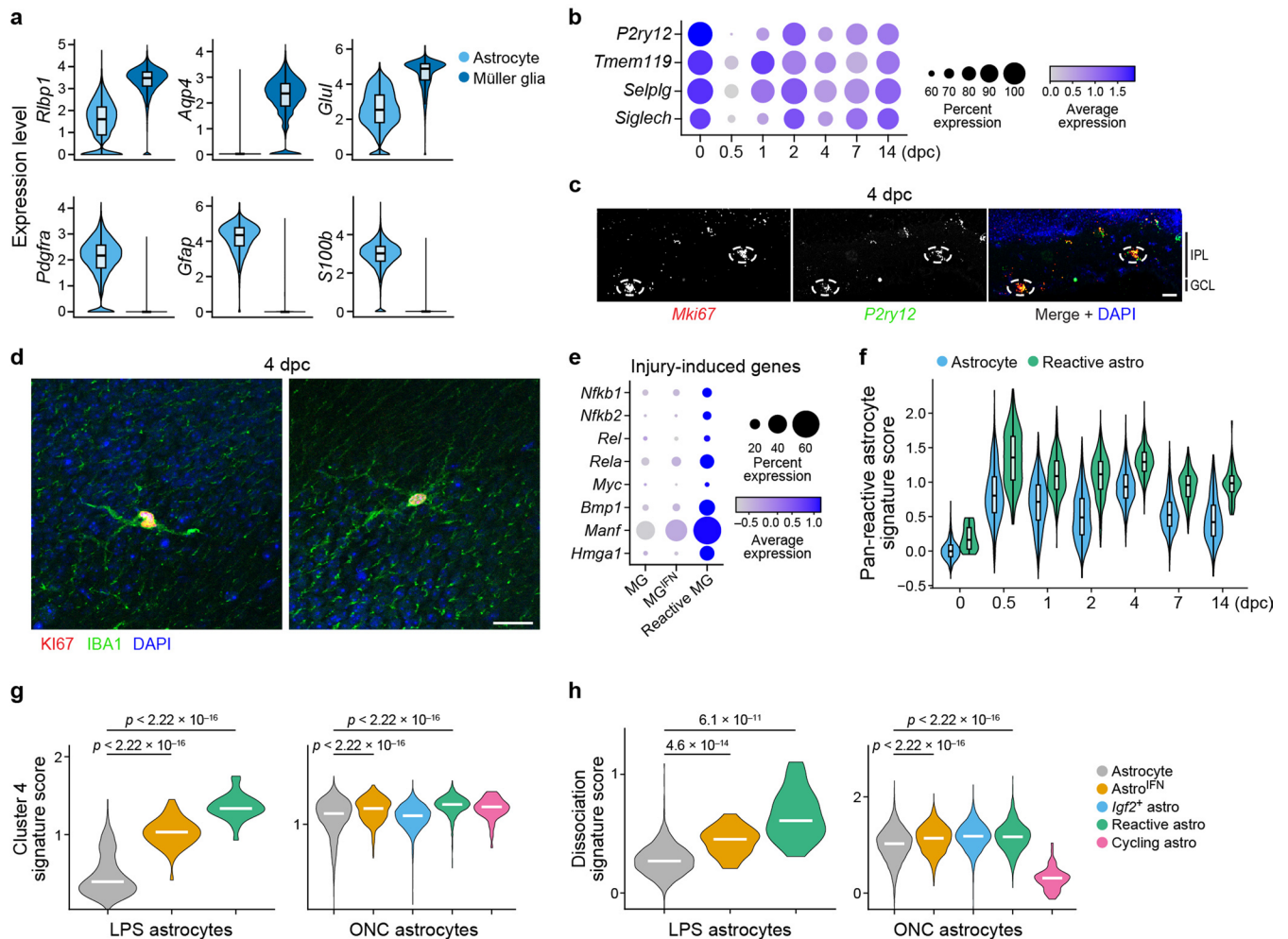
cells (dot color) of selected marker genes (columns) across 14 non-neuronal cell types (rows), plotted at each time point. **d**, UMAP for 21,275 cells profiled from mouse posterior eyecup at 0, 0.5, 1, 2 dpc, colored by time point. **e**, Fraction of expressing cells (dot size) and normalized expression in expressing cells (dot color) of selected marker genes (columns) across 12 identified cell types in the eyecup (rows). **f**, Endothelial cells collected from mouse eyecup, colored by expression of genes associated with choroidal Kdr^{hi} (left) and Kdr^{lo} (right) cells²⁰.



Extended Data Fig. 3 | Visualizing immune cells in the retina and eyecup.

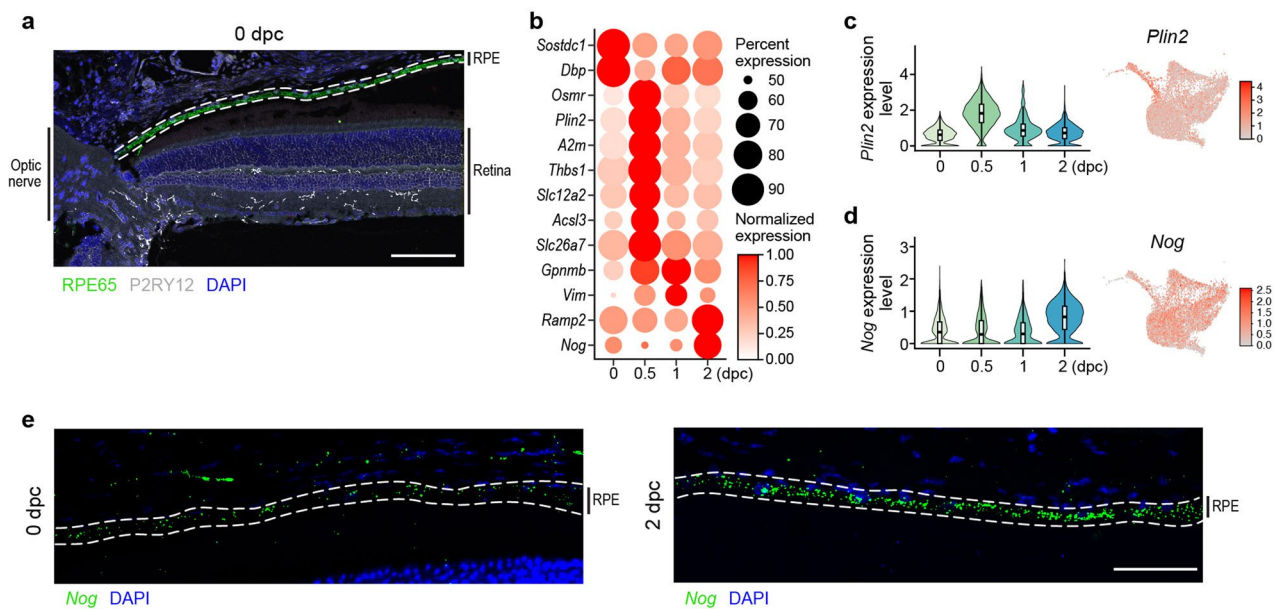
a, Fraction of expressing cells (dot size) and mean expression levels in expressing cells (dot color) of selected marker genes (columns) across 18 identified immune cell subsets (rows). **b,c**, Representative IHC on 0 and 0.5dpc retinal sections showing LY6G⁺ neutrophils that express MMP9 (red) and localize proximal to the optic nerve head (ONH) ($n = 3$ mice per time point) (**b**), and on 2dpc retinal whole-mounts from CCR2^{RFP/+} mice showing CCR2-RFP⁺ cells (red) in the GCL and IPL (**c**). Higher magnification inset of the outlined region in **c** is shown in Fig. 2d ($n = 2$). Scale bar, 50 μm . **d**, Representative IHC on 0dpc eyecup sections for IA-IE (MHC-II, magenta) and CD206 (green). Scale bar, 50 μm . Inset shows double positive cells, scale bar, 10 μm . BF, brightfield ($n = 2-3$ mice, representative of

two independent experiments). **e**, Representative image of smFISH on 2dpc sections showing *Ms4a7*⁺*Ccr2* cells (green) in the eyecup. This is a subset of the image presented in Fig. 5h. Scale bar, 50 μm . **f,g**, Representative images of IHC on eyecup whole-mounts (**f**) from CCR2^{RFP/+} mice showing that the majority of CCR2-RFP⁺ cells (red) in naïve eyecup are located posterior to the RPE, at the level of the choroid. ZO-1 (green) depicts tight junctions between individual RPE cells and nuclei are stained with Hoechst (blue) ($n = 2$ mice, representative of three independent experiments), and sections from 2dpc (**g**) showing that infiltrating CCR2-RFP⁺ cells (red) express the macrophage marker, IBA1 (green) ($n = 2$ mice). Arrowhead points to the RPE. Scale bars, 50 μm .



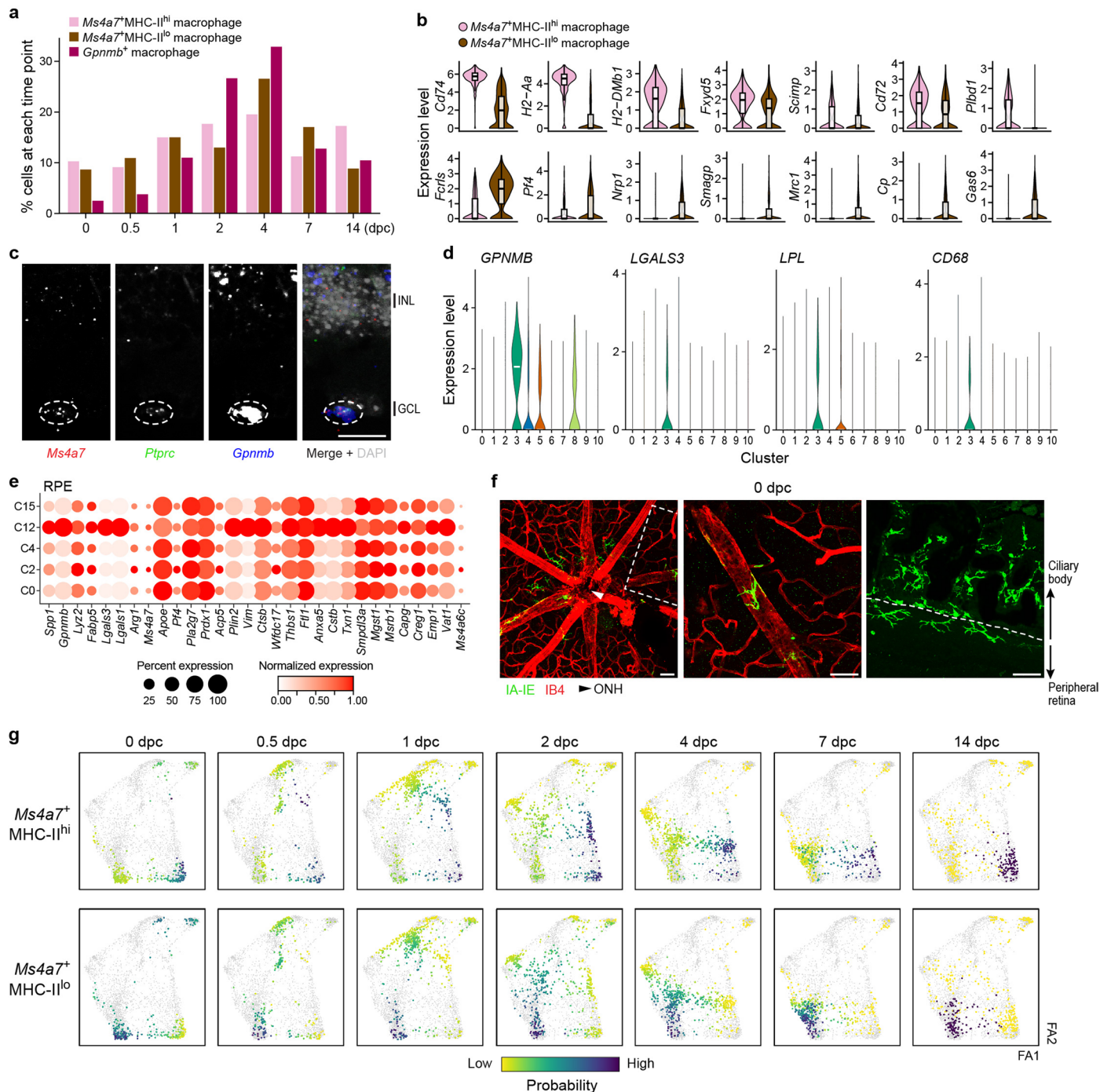
Extended Data Fig. 4 | Glial reactivation and microglial proliferation after ONC. **a**, Distribution of expression of genes differentially expressed between Müller glia (MG; $n = 54,565$ cells) and astrocytes ($n = 18,959$ cells). **b**, Fraction of expressing microglia cells (dot size) and mean expression levels in expressing cells (dot color) of microglia signature genes across time (0dpc ($n = 4,479$ cells); 0.5dpc ($n = 2,136$); 1dpc ($n = 1,712$); 2dpc ($n = 3,616$); 4dpc ($n = 2,950$); 7dpc ($n = 4,433$); 14dpc ($n = 5,233$)). **c,d**, Representative smFISH on 4dpc retinal sections (**c**) showing *P2ry12*⁺ microglia (green) expressing *Mki67* (red) ($n = 3$ mice), and IHC on 4dpc retinal whole-mounts (**d**) of *Ki67*⁺ (red) *IBA1*⁺ microglia (green) ($n = 3$ mice). Scale bars, 50 μm . **e**, Fraction of cells (dot size) in each MG subset, and mean expression level in expressing cells (dot color) of light and excitotoxin injury-induced genes³¹. **f**, Distribution of expression

scores for signature genes of pan-reactive astrocytes³⁵ across the astrocyte and astro^{IFN} subsets throughout the time course (Astrocyte/Reactive astro: 0dpc ($n = 1,009/17$ cells); 0.5dpc ($n = 586/299$); 1dpc ($n = 1,780/767$); 2dpc ($n = 2,268/439$); 4dpc ($n = 2,671/652$), 7dpc ($n = 2,051/396$); 14dpc ($n = 368/55$)). **g,h**, Distribution of expression scores for Cluster 4 ('inflammatory') signature from LPS-induced astrocytes³³ (**g**) and for a tissue dissociation signature (**h**) on astrocytes from LPS-induced neuroinflammation³³ classified to ONC astrocyte subsets (left) and across the ONC astrocyte subsets (right) (Student's *t*-test, one sided). Boxplots in **a** and **f** denote medians and IQRs; whiskers are the lowest datum still within 1.5 IQR of the lower quartile and the highest datum still within 1.5 IQR of the upper quartile.

**Extended Data Fig. 5 | ONC-induced expression changes in the RPE.**

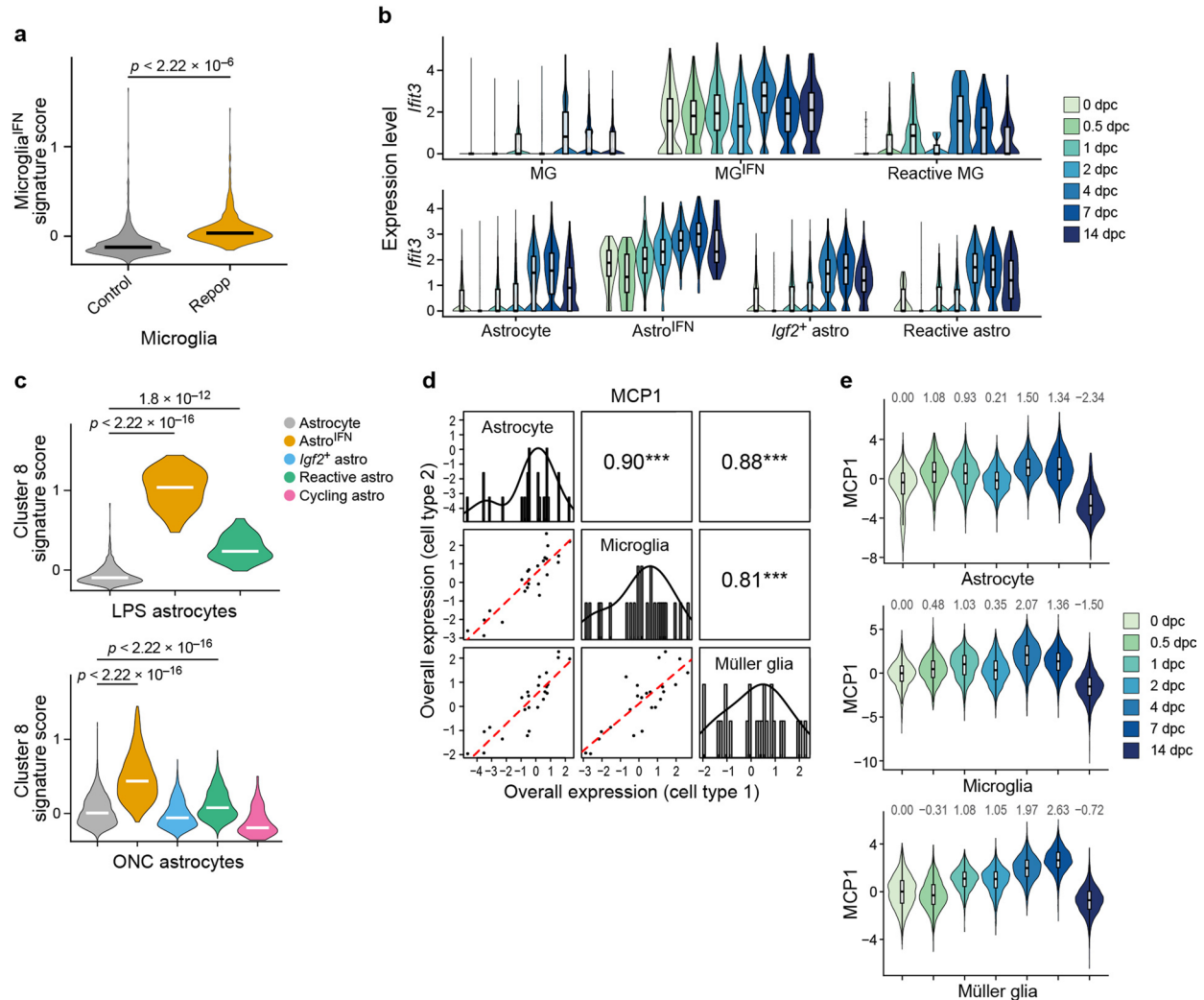
a, Representative image of IHC on ocular sections, depicting the RPE with specific staining (RPE65, green) in relation to the retina and optic nerve. Scale bar, 50 μ m. **b**, Fraction of expressing cells (dot size) and normalized expression level in expressing cells (dot color) of differentially expressed genes in the RPE between 0, 0.5, 1 and 2dpc. **c,d**, Distribution of expression of *Plin2* (**c**) and *Nog* (**d**)

on RPE cells by time (left; 0dpc (n = 2,605 cells); 0.5dpc (n = 1,746); 1dpc (n = 631); 2dpc (n = 3,031)) and across subsets (right). Boxplots denote medians and IQRs; whiskers are the lowest datum still within 1.5 IQR of the lower quartile and the highest datum still within 1.5 IQR of the upper quartile. **e**, Representative image of smFISH on 0 and 2dpc RPE for *Nog* (green) (n = 3 mice per time point). Scale bar, 50 μ m.



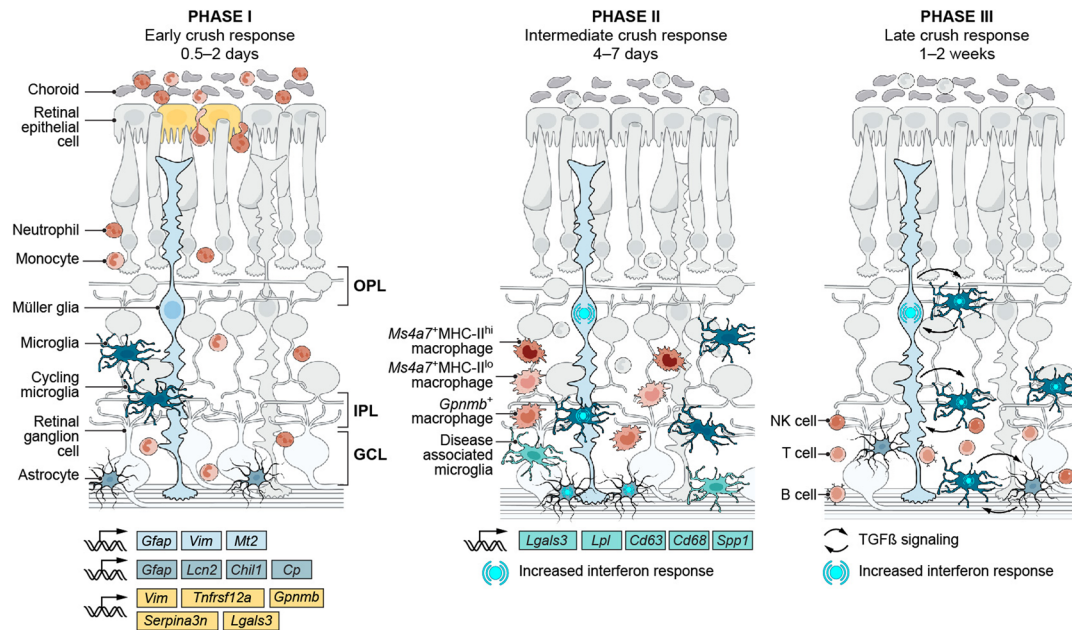
Extended Data Fig. 6 | Dynamics of resident and infiltrating mononuclear phagocytes in the retina, and conserved signature of *Gpnmb*⁺ macrophages. **a**, Changes in frequency of *Ms4a7*⁺MHC-II^{hi}, *Ms4a7*⁺MHC-II^{lo} and *Gpnmb*⁺ macrophages across 0, 0.5, 1, 2, 4, 7, and 14 dpc. **b**, Distribution of expression of genes associated with MHC-II^{hi} and MHC-II^{lo} BAMs²³ on retinal *Ms4a7*⁺MHC-II^{hi} (n = 741) and *Ms4a7*⁺MHC-II^{lo} macrophages (n = 1,406). Boxplots denote medians and IQRs; whiskers are the lowest datum still within 1.5 IQR of the lower quartile and the highest datum still within 1.5 IQR of the upper quartile. **c**, Representative image of smFISH on 7 dpc retina for *Gpnmb* (blue), *Ms4a7* (red) and *Ptprc* (green) (n = 3 mice). Scale bar, 25 μm. **d**, Distribution of expression of *Gpnmb*⁺ macrophage marker gene orthologs in immune cell scRNA-seq data from chronic lesions in human patients with multiple sclerosis⁴⁷. **e**, Fraction of expressing cells

(dot size) and normalized expression level in expressing cells (dot color) of the top 30 differentially expressed genes of *Gpnmb*⁺ macrophages across the RPE cell clusters. **f**, Representative IHC on uninjured (0 dpc) retinal whole-mounts showing perivascular and CB-adjacent IA-IE⁺ (green) cells. Blood vessels are labeled with IB4 (red) (representative of five independent experiments with n = 1-3 mice each). The middle panel shows a zoomed-in image of the perivascular macrophage in the inset of the left image. Scale bars, 50 μm. **g**, Force-directed layout view of monocyte and macrophage subsets with optimal transport analysis. Each dot is a cell, color-coded by ancestor probabilities for *Ms4a7*⁺MHC-II^{hi} (top row) and *Ms4a7*⁺MHC-II^{lo} macrophages (bottom row), as estimated by Waddington-OT⁸⁸.



Extended Data Fig. 7 | A co-regulated IFN-response program in the injured retina. **a**, Distribution of expression of genes differentially expressed in microglia^{IFN} by microglia repopulating the brain after depletion (Repop) compared to microglia from control brain⁵⁵ (Mann-Whitney U test, two sided). **b**, Distribution of *Ifit3* expression across time in MG (top) and astrocytes (bottom) across subsets. **c**, Distribution of a signature score of Cluster 8 ('ISG') astrocytes from LPS-induced neuroinflammation³³ in the LPS-induced astrocytes as classified to the ONC astrocyte subsets (left) and across the ONC astrocyte subsets (right) (Student's t-test, one sided). **d**, Off-diagonal panels: Comparison of overall expression scores (y and x axes) for each cell component of MCP1

(rows and columns, labels on diagonal) across the samples; lines correspond to linear fit. Pearson correlation (r) and significance ($***p < 0.001$; Pearson correlation t-test, one-sided) are shown in the panels above the diagonal. Diagonal panels: Distribution of overall expression scores for each cell type component, with kernel density estimates⁹¹. **e**, Distribution of MCP1 expression scores by astrocytes ($n = 18,956$ cells), microglia ($n = 20,000$ cells) and MG ($n = 19,998$ cells) across 0, 0.5, 1, 2, 4, 7 and 14 dpc. Numbers above violins indicate median expression scores. Boxplots in **b**, **e** denote medians and IQRs; whiskers are the lowest datum still within 1.5 IQR of the lower quartile and the highest datum still within 1.5 IQR of the upper quartile.



Extended Data Fig. 8 | Schematic model summarizing the tissue dynamics along the response to ONC. An inflammatory cascade is initiated early after injury (phase I), prior to RGC death, with activation of resident glia involving chemokine signals for leukocyte infiltration, which is observed in the oBRB and inner retina. At intermediate time points (phase II), concurrent with the peak rate of RGC death, infiltrating monocytes differentiate into distinct macrophage subsets, including *Ms4a7*⁺MHC-II^{hi}, *Ms4a7*⁺MHC-II^{lo} and *Gpnmb*⁺ macrophages.

In parallel, during this phase, a synchronous interferon response program is induced in astrocytes, Müller glia and microglia. The latter also express a disease-associated microglia signature, which overlaps with that of *Gpnmb*⁺ macrophages. Finally, at 1–2wpc (phase III), glial cell proportions begin to return to their baseline levels, with enriched interactions among them including TGFβ signaling, collectively indicating restoration of homeostasis.

Reporting Summary

Nature Portfolio wishes to improve the reproducibility of the work that we publish. This form provides structure for consistency and transparency in reporting. For further information on Nature Portfolio policies, see our [Editorial Policies](#) and the [Editorial Policy Checklist](#).

Statistics

For all statistical analyses, confirm that the following items are present in the figure legend, table legend, main text, or Methods section.

n/a Confirmed

- The exact sample size (n) for each experimental group/condition, given as a discrete number and unit of measurement
- A statement on whether measurements were taken from distinct samples or whether the same sample was measured repeatedly
- The statistical test(s) used AND whether they are one- or two-sided
Only common tests should be described solely by name; describe more complex techniques in the Methods section.
- A description of all covariates tested
- A description of any assumptions or corrections, such as tests of normality and adjustment for multiple comparisons
- A full description of the statistical parameters including central tendency (e.g. means) or other basic estimates (e.g. regression coefficient) AND variation (e.g. standard deviation) or associated estimates of uncertainty (e.g. confidence intervals)
- For null hypothesis testing, the test statistic (e.g. F , t , r) with confidence intervals, effect sizes, degrees of freedom and P value noted
Give P values as exact values whenever suitable.
- For Bayesian analysis, information on the choice of priors and Markov chain Monte Carlo settings
- For hierarchical and complex designs, identification of the appropriate level for tests and full reporting of outcomes
- Estimates of effect sizes (e.g. Cohen's d , Pearson's r), indicating how they were calculated

Our web collection on [statistics for biologists](#) contains articles on many of the points above.

Software and code

Policy information about [availability of computer code](#)

Data collection

The demultiplexed FASTQ files from the sequencing center were shared with us via FTP

Data analysis

Cell Ranger 2.1.0 (10x Genomics) was used for read demultiplexing, alignment to the mouse genome and unique molecular identifier (UMI) counting and collapsing. The top 6,000 cells from each experiment with the largest number of UMI were used for further analysis. In total, 121,309 cells expressing at least 400 genes per cell were retained for downstream analysis. scSphere was used to merge all 121,309 cells from different time points by taking time after crush and mouse strain as the batch vectors. The Seurat package was used for clustering analysis, differential expression analysis, and UMAP visualization. Velocyto and scVelo were used for RNA velocity analysis. The Waddington-OT package was used to infer the developmental trajectory of macrophages and microglia. DIALOGUE was used to infer multicellular programs. Customized code was used to infer ligand-receptor interactions based on a manually curated ligand-receptor database.

For manuscripts utilizing custom algorithms or software that are central to the research but not yet described in published literature, software must be made available to editors and reviewers. We strongly encourage code deposition in a community repository (e.g. GitHub). See the Nature Portfolio [guidelines for submitting code & software](#) for further information.

Data

Policy information about [availability of data](#)

All manuscripts must include a [data availability statement](#). This statement should provide the following information, where applicable:

- Accession codes, unique identifiers, or web links for publicly available datasets
- A description of any restrictions on data availability
- For clinical datasets or third party data, please ensure that the statement adheres to our [policy](#)

Data generated during this study have been deposited in Gene Expression Omnibus (GEO) under accession number GSE199317. The data can be visualized in the Broad Institute Single Cell Portal (https://singlecell.broadinstitute.org/single_cell) under accession SCP1785.

Human research participants

Policy information about [studies involving human research participants and Sex and Gender in Research](#).

Reporting on sex and gender

Use the terms sex (biological attribute) and gender (shaped by social and cultural circumstances) carefully in order to avoid confusing both terms. Indicate if findings apply to only one sex or gender; describe whether sex and gender were considered in study design whether sex and/or gender was determined based on self-reporting or assigned and methods used. Provide in the source data disaggregated sex and gender data where this information has been collected, and consent has been obtained for sharing of individual-level data; provide overall numbers in this Reporting Summary. Please state if this information has not been collected. Report sex- and gender-based analyses where performed, justify reasons for lack of sex- and gender-based analysis.

Population characteristics

Describe the covariate-relevant population characteristics of the human research participants (e.g. age, genotypic information, past and current diagnosis and treatment categories). If you filled out the behavioural & social sciences study design questions and have nothing to add here, write "See above."

Recruitment

Describe how participants were recruited. Outline any potential self-selection bias or other biases that may be present and how these are likely to impact results.

Ethics oversight

Identify the organization(s) that approved the study protocol.

Note that full information on the approval of the study protocol must also be provided in the manuscript.

Field-specific reporting

Please select the one below that is the best fit for your research. If you are not sure, read the appropriate sections before making your selection.

Life sciences Behavioural & social sciences Ecological, evolutionary & environmental sciences

For a reference copy of the document with all sections, see [nature.com/documents/nr-reporting-summary-flat.pdf](https://www.nature.com/documents/nr-reporting-summary-flat.pdf)

Life sciences study design

All studies must disclose on these points even when the disclosure is negative.

Sample size

No statistical methods were used to determine sample size. Sample sizes were chosen based on previous publications and on pilot experiments.

Data exclusions

Retinas were excluded from analysis if optic nerve crush was incomplete, or if signs of damage or bleeding were evident upon dissection. No data was specifically excluded, but filtering was performed as described in the Methods section to exclude cells (cell barcodes) of low quality.

Replication

Experiments were performed with biological and technical replicates, with similar results.

Randomization

Age- and genotype-matched mice were randomized for in vivo experiments with several groups.

Blinding

The computational analysis pipeline was identical for all processed samples, and intended to be unbiased, so blinding was not relevant.

Reporting for specific materials, systems and methods

We require information from authors about some types of materials, experimental systems and methods used in many studies. Here, indicate whether each material, system or method listed is relevant to your study. If you are not sure if a list item applies to your research, read the appropriate section before selecting a response.

Materials & experimental systems

- n/a Involved in the study
- Antibodies
- Eukaryotic cell lines
- Palaeontology and archaeology
- Animals and other organisms
- Clinical data
- Dual use research of concern

Methods

- n/a Involved in the study
- ChIP-seq
- Flow cytometry
- MRI-based neuroimaging

Antibodies

Antibodies used

A detailed list is included in Supplementary Table 4.

Validation

Commercially-available antibodies were validated by the manufacturers. We tested newly-used antibodies including controls where the primary antibody was omitted. For new lots of MC-21, blood monocyte depletion was confirmed with flow cytometry. For flow cytometry experiments, unstained and single-stained antibody controls were routinely used.

Animals and other research organisms

Policy information about [studies involving animals](#); [ARRIVE guidelines](#) recommended for reporting animal research, and [Sex and Gender in Research](#)

Laboratory animals

Experiments were carried out in adult mice, 6-16 weeks of age and included both males and females. Mice were purchased from Jackson Laboratory or bred in-house. The following mouse strains were used:

1. C57BL/6J (JAX #000664)
2. Vglut2-ires-cre (Slc17a6tm2(cre)Lowl/J) crossed to the cre-dependent reporter Thy1-stop-YFP Line#15 (B6.Cg-Tg(Thy1-EYFP)15Jrs/J)
3. CCR2RFP (B6.129(Cg)-Ccr2tm2.1fc/J; JAX #017586), crossed to C57BL/6J mice to generate heterozygotes.

Wild animals

The study did not involve wild animals.

Reporting on sex

The majority of C57BL/6J mice were male. Vglut2-Cre-YFP male and female mice were pooled for scRNA-seq experiments. Male and female CCR2-RFP mice were used for validation experiments.

Field-collected samples

N/A

Ethics oversight

All animal experiments were approved by the Institutional Animal Care and Use Committees (IACUC) at Harvard University and Boston Children's Hospital.

Note that full information on the approval of the study protocol must also be provided in the manuscript.

Flow Cytometry

Plots

Confirm that:

- The axis labels state the marker and fluorochrome used (e.g. CD4-FITC).
- The axis scales are clearly visible. Include numbers along axes only for bottom left plot of group (a 'group' is an analysis of identical markers).
- All plots are contour plots with outliers or pseudocolor plots.
- A numerical value for number of cells or percentage (with statistics) is provided.

Methodology

Sample preparation

Mice were intracardially perfused with PBS. For retina: Eyes were dissected in AMES solution (equilibrated with 95% O₂/5% CO₂). Retinas, separated from eyecup and ciliary body, were digested in papain, and dissociated to single cell suspensions using manual trituration in ovomucoid solution. Cells were spun down at 450 g for 8 minutes and resuspended in AMES+4 BSA to a concentration of 10 million cells per 100 ml. For RPE, we adapted a protocol based on Fernandez-Godino et al. Briefly, eyecups were dissected in Hank's Balanced Salt Solution (HBSS)- with HEPES and incubated in 0.25% trypsin/EDTA for 45 minutes at 37°C, after which RPE sheets were released by manual shaking into 20% fetal bovine serum (FBS) in HBSS+ with HEPES, spun down at 340 g for 2 minutes and

	incubated in 0.05% Trypsin/EDTA for 10 minutes at 37°C. Cells were washed, resuspended and triturated 50 times in 5% FBS/HBSS+ with HEPES and filtered for staining and cell sorting.
Instrument	Cells were sorted on a MoFlo Astrios Cell Sorter (Beckman Coulter).
Software	Data were collected with Summit (version 6.3) and analyzed with FlowJo software (TreeStar).
Cell population abundance	We enriched for the populations of interest by antibody-mediated sorting. CD45+ immune cells were ~0.5%-1%; GLAST+ Muller glia were ~3% and astrocytes were ~0.2% of the total retinal cells, in line with their published abundances. Since we did not have a good surface antibody to sort RPE cells, they were sorted based on FSC/SSC gates. We validated that sorted fractions were enriched of RPE cells in preliminary experiments.
Gating strategy	Cells were first gated on FSC-H/SSC-H. Singlets were selected based on SSC-H/SSC-W and live cells were selected based on calcein blue staining. Subsequent positive and negative populations were based on unstained and single stained controls.

Tick this box to confirm that a figure exemplifying the gating strategy is provided in the Supplementary Information.